

# Numerical Investigation of Inverse Magnus Effect on a Circular Cylinder by Controlling Azimuthal Circulation Distribution

Submitted to the Graduate School of Natural and Applied Sciences  
in partial fulfillment of the requirements for the degree of

Master of Science

in Mechanical Engineering

by

Acar Çelik

ORCID 0000-0002-2091-4753

April, 2021

This is to certify that we have read the thesis **Numerical Investigation of Inverse Magnus Effect on a Circular Cylinder by Controlling Azimuthal Circulation Distribution** submitted by **Acar Çelik**, and it has been judged to be successful, in scope and in quality, at the defense exam and accepted by our jury as a MASTER'S THESIS.

**APPROVED BY:**

**Advisor:** **Assoc. Prof. Dr. Sercan Acarer**  
İzmir Kâtip Çelebi University

**Co-advisor:** **Assoc. Prof. Dr. Beni Cukurel**  
Technion – Israel Institute of Technology

**Committee Members:**

**Assoc. Prof. Dr. Mehmet Akif Ezan**  
Dokuz Eylül University

**Assoc. Prof. Dr. Z. Haktan Karadeniz**  
İzmir Kâtip Çelebi University

**Asst. Prof. Dr. Ian Jacobi**  
Technion – Israel Institute of Technology

**Date of Defense: April 22, 2021**

# Declaration of Authorship

I, **Acar Çelik**, declare that this thesis titled **Numerical Investigation of Inverse Magnus Effect on a Circular Cylinder by Controlling Azimuthal Circulation Distribution** and the work presented in it are my own. I confirm that:

- This work was done wholly or mainly while in candidature for the master's degree at this university.
- Where any part of this thesis has previously been submitted for a degree or any other qualification at this university or any other institution, this has been clearly stated.
- Where I have consulted the published work of others, this is always clearly attributed.
- Where I have quoted from the work of others, the source is always given. This thesis is entirely my own work, with the exception of such quotations.
- I have acknowledged all major sources of assistance.
- Where the thesis is based on work done by myself jointly with others, I have made clear exactly what was done by others and what I have contributed myself.

Signature:

---

Date: 21.05.2021

---

# Numerical Investigation of Inverse Magnus Effect on a Circular Cylinder by Controlling Azimuthal Circulation Distribution

## Abstract

Magnus effect is a phenomenon that occurs in specific conditions. In order to observe this phenomenon, it is needed to have a spinning body (usually sphere or cylinder) immersed in a flow medium. Flow on the retreating side (the side of the body moving with flow) is guided towards the rotational direction and creates a reaction force (aka lift) acting on the opposite direction. Contrarily, the direction of the force is just the opposite in the inverse Magnus effect. At critical Reynolds number and the spin ratio, flow on the retreating side tends to be laminar, which causes early separation. On the other hand, flow on the advancing side (the side of the body moving with flow) tends to be turbulent, delaying a separation. As a result, the flow is guided against the rotational direction in the advancing side more dominantly. These physical responses are generally used for circulation control in airfoils. In this study, flow over a cylinder is numerically investigated with the control of azimuthal circulation distribution by local moving surfaces. The aim is to reach the ordinary and inverse Magnus forces, observing the influence of the configuration of rotating surfaces. To achieve this, a two-dimensional numerical model was generated with  $k-kl-\omega$  turbulence model. Two novel methods were developed for determining separation and transition locations. Employing these criteria, the relationship between the separation, the transition, and

the Magnus phenomenon were emphasized. Moreover, an optimization study was carried out to determine the locations of actuators for the maximal inverse Magnus force. As a result, 466% lift-to-drag coefficient ( $\overline{C_L}/\overline{C_D}$ ) increment was obtained after the gradient based optimization when the comparison is performed between fully and partially rotating cylinders. As a conclusion, the output of the current study is expected to enable a better understanding on the topic. Thus, it aims to promote the use of the inverse Magnus effect for manipulating lift and drag forces acting on bodies exposed to flow, such as (but not limited to) airfoils, rotors of Flettner ships, crafts and possibly even some critical buildings. Additionally, the methodology of separation and (to a lesser extent) transition criteria is critical and compelling for the rotating cylinders or flows where any wall is moving opposite to the flow.

**Keywords:** Inverse Magnus effect, cylinder, circulation, lift force, turbulence

# Ters Magnus Etkisinin Çevresel Sirkülasyon Dağılımı Kontrolü ile Dairesel Silindir Üzerinde Sayısal Olarak İncelenmesi

## ÖZ

Magnus etkisi, belirli koşullarda ortaya çıkan fiziksel bir olgudur. Bu fenomeni gözlemlemek için, bir akış ortamına daldırılmış dönen bir gövdeye (genellikle küre veya silindir) sahip olmak gerekir. Geri çekilme tarafındaki akış (gövdenin akışla aynı yönde hareket eden tarafı) dönüş yönünde yön değiştirir ve ters yönde etki eden bir tepki kuvveti (diğer bir deyişle kaldırma kuvveti) oluşturur. Ters Magnus etkisinde ise kuvvet tam zıt yönde oluşmaktadır. Kritik Reynolds sayısı ve dönme oranı aralıklarında, geri çekilen taraftaki akış laminer olma eğilimindedir ve bu da erken akış ayrılmasına neden olur. Öte yandan, ilerleyen taraftaki (gövdenin akışla ters yönde hareket eden tarafı) akış, türbülanslı olma eğilimindedir ve bu durum akış ayılmasını geciktirir. Sonuç olarak, akış daha baskın olarak ilerleyen tarafta dönme yönüne karşı yönlendirilir. Bu fiziksel tepkiler genellikle kanat profillerinde sirkülasyon kontrolü için kullanılmaktadır. Bu çalışmada, yerel hareketli yüzeyler yardımıyla, çevresel sirkülasyon dağılımının kontrolü ile bir silindir üzerindeki akış sayısal olarak incelenmiştir. Amaç, hareketli yüzeylerin konfigürasyonunun etkisini gözlemleyerek normal ve ters Magnus kuvvetlerine ulaşmaktır. Bu amaçla,  $k-kl-\omega$  türbülans modeli kullanılarak iki boyutlu bir sayısal model oluşturulmuştur. Akış ayrılması ve türbülansa geçiş konumlarını belirlemek için iki farklı yöntem geliştirilmiştir. Bu

kriterler kullanılarak akış ayrılması, türbülansa geçiş ve Magnus fenomeni arasındaki ilişki vurgulanmıştır. Ek olarak, belirtilen koşullarda maksimum ters Magnus kuvvetini elde etmek için hareketli yüzeylerin konumları üzerinden bir optimizasyon çalışması gerçekleştirilmiştir. Sonuç olarak, gradyen bazlı optimizasyonun ardından, tamamen ve kısmen dönen silindirler arasında karşılaştırma yapıldığında kaldırma ve sürüklenme katsayılarının oranında ( $\overline{C_L}/\overline{C_D}$ ) %466'lık bir artış elde edildi. Sonuç olarak, mevcut çalışmanın çıktısının konunun daha iyi anlaşılmasını sağlaması beklenmektedir. Bu bağlamda, kanat profilleri, Flettner gemilerinin rotorları, hava araçları ve hatta bazı kritik yapılar gibi akışa maruz kalan gövdelere etki eden kaldırma ve sürüklenme kuvvetlerini manipüle etmek için ters Magnus etkisinin kullanımını teşvik etmeyi amaçlamaktadır. Ek olarak, akış ayrılması ve (daha az ölçüde) türbülansa geçiş kriterleri için oluşturulan metodolojilerin, herhangi bir duvarın akışın tersine hareket ettiği dönen silindirlerde veya akışlarda oldukça kritik ve zorlu olduğu gözlemlenmiştir.

**Anahtar Kelimeler:** Ters Magnus etkisi, silindir, sirkülasyon, kaldırma kuvveti, türbülans

*To my beloved ones,*



# Acknowledgement

I would like to thank my co-advisors Dr. Sercan Acarer and Dr. Beni Cukurel for their selfless support and mentorship in the scope of this work and my career. Their excellent guidance and friendship throughout this work is more than invaluable. I also thank Dr. Ian Jacobi for his superior contribution to this work. His knowledge and assistance provided me to carry this study on a further point.

I would like to thank my committee members, Dr. Mehmet Akif Ezan and Dr. Ziya Haktan Karadeniz for their valuable contributions and support. I would also like to thank Turbomachinery and Heat Transfer laboratory members who made this journey more fruitful, including Boris Leizeronok, Dr. Tapish Agarwal, Yair Lange, Ron Miezner, Dr. Iliya Romm, David Linsky, Michael Palman, Dr. Slava Losin, Liat Sivan, Salman Nbwani and Alex Kleiman. Their awesome friendship and contribution to my academic and personal growth is priceless. I also would like to acknowledge all my friends. I always feel their endless support.

Most importantly, I would like to thank to my mother Huriye Çelik, my father Ercan Çelik, my brother Şafak Çelik and my love Beyza Özer. I feel fortunate and grateful for their unconditional support, perseverance and understanding.

# Table of Contents

Declaration of Authorship .....	ii
Abstract .....	iii
Öz .....	v
Acknowledgment .....	viii
List of Figures .....	xi
List of Tables .....	xiii
List of Abbreviations .....	xiv
List of Symbols .....	xv
<b>1 Background .....</b>	<b>1</b>
1.1 Outline of aerodynamic forces .....	1
1.2 Cross-flow aerodynamics of a rotating body .....	3
1.2.1 Magnus effect .....	3
1.2.2 Inverse Magnus effect .....	5
<b>2 Introduction .....</b>	<b>7</b>
<b>3 Numerical Method .....</b>	<b>13</b>
3.1 Selection of method .....	13
3.1.1 Large eddy simulation (LES) .....	13
3.1.2 $\gamma - Re_\theta$ model (Transition – SST model) .....	14
3.1.2 Transition k-kl- $\omega$ model .....	15
3.2 Computational domain .....	15
3.3 Grid structure .....	16
3.4 Solution method .....	17

3.5	Boundary and initial conditions .....	18
3.6	Temporal resolution analysis .....	18
3.7	Validation .....	20
3.7.1	Stationary cylinder .....	20
3.7.2	Rotating cylinder .....	22
<b>4</b>	<b>Results .....</b>	<b>24</b>
4.1	Development of transition onset and separation point criteria for arbitrary circulation distribution .....	24
4.1.1	Transition criterion .....	25
4.1.2	Separation criterion .....	30
4.2	Inverse Magnus effect by circulation control using partially rotating boundaries .....	40
4.2.1	Comparison of fully and partially rotating cylinders .....	42
4.2.2	Sensitivity analysis and gradient descent optimization of actuator configurations .....	45
<b>5</b>	<b>Conclusion .....</b>	<b>52</b>
	<b>References .....</b>	<b>54</b>
	<b>Appendices .....</b>	<b>59</b>
	Appendix A Experimental setup design for future work.....	60
	Appendix B Validation of optimization methods.....	63
	<b>Curriculum Vitae .....</b>	<b>66</b>

# List of Figures

Figure 1.1	Aerodynamic forces on airfoil .....	1
Figure 1.2	Surface pressure and shear stress .....	2
Figure 1.3	Magnus effect .....	4
Figure 1.4	Inverse Magnus effect .....	5
Figure 2.1	Force inclination angle with respect to direction of the stream velocity reproduced from [3] .....	8
Figure 2.2	Representative image for the Krahn's setup .....	9
Figure 2.3	Change of lift coefficient with spin ratio, reproduced from [9] (a-f: Re = 3.58E+04 - 12.8E+04, g-m: Re = 15.2E+04 - 36.5E+04, n-p: Re = 42E+04 - 50.1E+04) .....	10
Figure 3.1	Computational domain .....	15
Figure 3.2	Mesh structure .....	17
Figure 3.3	(a) Change of the time-averaged drag coefficient with respect to Reynolds number. (b) Variation of the time-averaged separation angle results. [1,24,25,30,31,32,33] .....	21
Figure 3.4	Skin friction coefficients around the cylinder [33] .....	22
Figure 3.5	Validation study for fully rotating cylinder at constant Re = 128k. Time-averaged lift ( $\overline{C_L}$ ) and drag ( $\overline{C_D}$ ) coefficients are indicated with spin ratio ( $\alpha$ ) for <i>Transition-SST</i> and <i>k-kl-<math>\omega</math></i> turbulence models. [9] .....	23
Figure 4.1	Appropriate conditions for inverse Magnus effect [10] .....	24
Figure 4.2	Transition onset angles calculated by the current criteria calculated by time-averaged turbulence properties, $\overline{\theta_{tr}}$ , with respect to $y^+$ . (a) Stationary cylinder, (b) fully rotating cylinder .....	29
Figure 4.3	Demonstration of flow over moving walls at, (a) downstream-moving wall, (b) upstream-moving wall [41].....	31

Figure 4.4	$\overline{\theta_e}$ with respect to gradients of mean displacement thickness in (a), and mean pressure coefficient in (b) at the top side of cylinder. Formulation of $\overline{\theta_e}$ is given in Equation 4.14.....	33
Figure 4.5	$\overline{\theta_e}$ with respect to criteria outputs .....	36
Figure 4.6	Example of pressure gradient distribution .....	37
Figure 4.7	Monte Carlo simulations and distribution of separation angles .....	38
Figure 4.8	Circular cylinder inside the flow domain with the boundary conditions. Stationary cylinder with enumerated 4 actuators rotating clockwise direction. The first actuator is located where the flow separates on the top of the stationary cylinder ( $(\overline{\theta_s})_t = 81^\circ$ ).....	41
Figure 4.9	Fully and partially rotating cylinder cases are compared in time-averaged aerodynamic force coefficients. (a) Lift coefficient, (b) drag coefficient, (c) lift-to-drag coefficient. The x-axis corresponds weighted-average wall circulation (Equation 4.22).....	43
Figure 4.10	$\overline{C_L}/\overline{C_D}$ with respect to step size as a result of PGD method .....	47
Figure 4.11	Mean streamlines with the locations of transition onset and separation. ....	48
Figure A.1	Elements of the experimental setup (1) Water tunnel test section, (2) Laser, (3) Computer, (4) High speed camera, (5) Force balance rod, (6) Load cell, (7) Amplifier, (8) Balancing table, (9) Stator, (10) Rotor (actuator), (11) DC-Motor) .....	60
Figure A.2	(a) Cross section of the system, (b) Detailed look of sealing and driver section, (c) Experimental test section.....	62
Figure B.1	Comparison of paths: blue line is Projected gradient descent method; red line is Frank-Wolfe method; black line is optimal path. G and $\gamma$ are adjusted.....	64

# List of Tables

Table 3.1	Convergence of each mesh compared to the maximum resolution (235k elements) .....	16
Table 3.2	Physical properties of water at 25°C, 1 atm .....	18
Table 3.3	Time resolution convergence by the lowest Courant number case (Co = 0.1).....	19
Table 4.1	Separation angles, $(\overline{\theta_s})_t$ found by MRS criterion at stationary and fully rotating cases on the top side of the cylinder .....	33
Table 4.2	Separation criteria expressions and RMS/average of outputs at minimum $\overline{\theta_e}$ .....	34
Table 4.3	Separation and transition angles for the test cases. MRS criteria is only used for the receding (top) side. Current separation and transition onset criteria outputs are shown both receding and advancing (bottom) sides with the calculation uncertainties .....	39
Table 4.4	Simulation outputs of compared cases (fully and partially rotating cylinders) at $\overline{\Gamma_w} = 0.35$ . .....	44
Table 4.5	Comparison of selected 5 cases with different variables .....	50

# List of Abbreviations

APG	Adverse Pressure Gradient
C.V.	Control Volume
DNS	Direct Numerical Simulation
DPIV	Digital Particle Image Velocimetry
FPG	Favorable Pressure Gradient
LES	Large Eddy Simulation
MRS	Moore, Rott and Sears
ORCID	Open Researcher and Contributor ID
PGD	Projected Gradient Descent
PRESTO	Pressure Staggering Option
RANS	Reynolds Averaged Navier Stokes
RMS	Root Mean Square
SIMPLEC	Semi-Implicit Method for Pressure Linked Equations-Consistent
SST	Shear Stress Transport
URANS	Unsteady Reynolds Averaged Navier Stokes
err	Error
out	Outlet
w	Wall

# List of Symbols

$A$	area [m <sup>2</sup> ]
$a$	superscript for separation criterion
$A_a$	surface area of the attached flow region [m <sup>2</sup> ]
$A_s$	surface area of the separated flow region [m <sup>2</sup> ]
$b$	superscript for separation criterion, bias error, bottom side
$C$	separation criterion
$Co$	Courant Number
$C_f$	skin friction coefficient
$C_t$	transition criterion
$C_\mu$	model constant
$\overline{C_D}$	time-averaged drag coefficient
$\overline{C_L}$	time-averaged lift coefficient
$\overline{C_p}$	time-averaged pressure coefficient
$D$	diameter [m]
$dA$	differential area [m <sup>2</sup> ]
$(e_{C_D})_s$	spatial error for drag coefficient
$(e_{C_D})_t$	temporal error for drag coefficient
$(e_{C_L})_s$	spatial error for lift coefficient
$(e_{C_L})_t$	temporal error for lift coefficient
$F$	force [N]
$F_D$	drag force [N]
$F_L$	lift force [N]



$f_s$	fraction of separated region
$I$	turbulence intensity [%]
$i$	spatial index
$k$	turbulent kinetic energy [ $\text{m}^2/\text{s}^2$ ]
$l$	turbulent length scale [m]
$\dot{m}$	mass flow rate [kg/s]
$N$	rotational velocity [rpm]
$n$	normal direction
$P$	pressure [Pa]
$p$	precision error
$Re$	Reynolds Number
$Re^*$	modified Reynolds number
$s$	minimization vector, separation
$t$	flow time [s], top side
$t^*$	non-dimensional flow time
$U$	reference velocity [m/s]
$u$	velocity in x-direction [m/s]
$U_\infty$	free stream velocity [m/s]
$U_\theta$	wall surface tangential velocity [m/s]
$u'$	RMS of turbulent velocity fluctuations [m/s]
$v$	velocity in y-direction [m/s]
$x$	x-direction [m]
$x^+$	non-dimensional wall distance in steamwise direction
$y$	y-direction [m], first grid layer height [m]
$y^+$	non-dimensional wall distance in normal direction
$z^+$	non-dimensional wall distance in spanwise direction
$\alpha$	spin ratio

$\Gamma$	circulation [m <sup>2</sup> /s]
$\gamma$	step size for optimization
$\overline{\Gamma_w}$	area-weighted averaged wall circulation
$\Delta t$	time-step [s]
$\Delta t^*$	non-dimensional time-step
$\Delta \theta$	angular difference [°]
$\Delta x$	grid height [m]
$\delta^*$	displacement thickness [m]
$\overline{\delta^*}$	time-averaged displacement thickness [m]
$\theta$	angle [°], tangential component
$\overline{\theta_e}$	time-averaged angle error
$\overline{\theta_s}$	time-averaged separation angle [°]
$\overline{\theta_{sp}}$	angle of the time-averaged front stagnation point [°]
$\overline{\theta_{tr}}$	time-averaged transition onset angle [°]
$\overline{\theta_{sb}}$	time-averaged bottom separation angle [°]
$\overline{\theta_{st}}$	time-averaged top separation angle [°]
$\overline{\theta_{trb}}$	time-averaged bottom transition onset angle [°]
$\overline{\theta_{trt}}$	time-averaged top transition onset angle [°]
$\mu$	dynamic viscosity [kg/ms]
$\mu_t$	turbulent viscosity [kg/ms]
$\rho$	density [kg/m <sup>3</sup> ]
$\sigma$	sigma
$\sigma_{C_D}$	deviation of drag coefficient
$\sigma_{C_L}$	deviation of lift coefficient
$\tau$	shear stress [Pa]
$\tau_w$	wall shear stress [Pa]
$\omega$	specific dissipation rate [1/s]

# Chapter 1

## Background

### 1.1 Outline of aerodynamic forces

Interaction among the body and the fluid has always been the foundation in aerodynamics. This relationship is considered from the kinetics point of view by majority. A body immersed in a flow media is exposed different fundamental forces called aerodynamic forces. The effect of aerodynamics forces may only be come out by the motion of at least either body or fluid. In order to understand these forces, the pressures acting on the body must be known. They are simply caused by the pressure on the surface of the body and the physical properties of the fluid. These corresponds normal and shear forces, respectively.

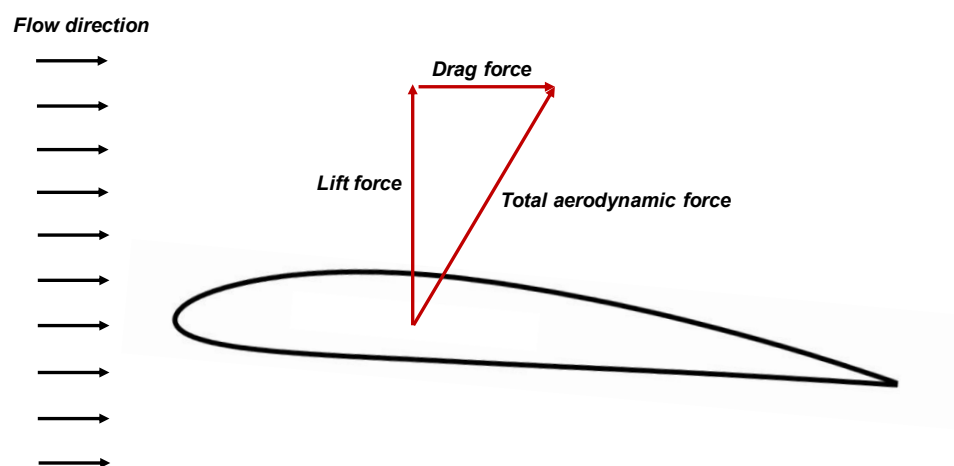


Figure 1.1: Aerodynamic forces on airfoil

Relative motion between body and the fluid points out the direction of the aerodynamic forces. These are divided into two components, such as the streamwise drag force as well as the lift force which is the normal force with respect to the course of relative flow direction. In Figure 1.1., referred forces are presented.

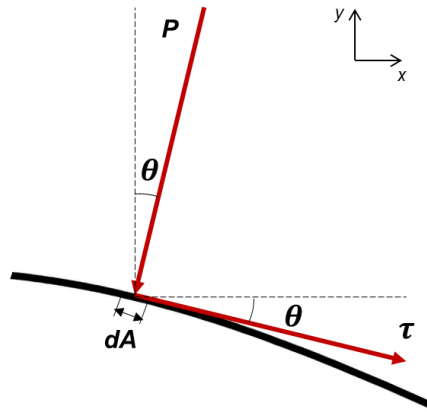


Figure 1.2: Surface pressure and shear stress

Lift and drag forces are defined by the integration of surface pressure and shear stress throughout the body. Equations 1.1. and 1.2. are generated regarding Figure 1.2.

$$F_L = \int (-P \cos \theta - \tau \sin \theta) dA \quad (1.1)$$

$$F_D = \int (-P \sin \theta + \tau \cos \theta) dA \quad (1.2)$$

In Equation 1.1. and Equation 1.2., formulation of drag and lift forces are indicated.  $P$ ,  $\tau$ ,  $\theta$ ,  $dA$  corresponds surface pressure, shear stress, flow direction angle and differential area, respectively.

## 1.2 Cross-flow aerodynamics of rotating body

External flows have been considerably crucial for so long in different branches of science and technology. One of the baseline field of studies is cross-flow aerodynamics when this kind of flows considered. Essentially, investigations about the flow over a circular cylinder are utilized to understand the constituents of flow characteristics as well as to verify experimental and numerical studies. With this motivation, numerous efforts were given on this topic. Physical properties, pressure and velocity distributions, flow types and patterns are predominantly effective on the aerodynamics of a body. In general sense, two types of problems are encountered in particularly flow over a cylinder, such as, stationary body as well as rotating body.

In stationary cylinder problems, symmetrical pressure and velocity distributions are obtained in the mean flow characteristics. Especially, this symmetrical mean pressure distribution causes zero lift force onto the cylinder in overall stance. Nevertheless, drag force increases with the Reynolds number until its supercritical range is reached. After that, it suddenly decreases which the phenomenon called drag crisis [1]. Drag forces can only be controlled by the parameters in which are inside the Reynolds number ( $Re = \rho U_{\infty} D / \mu$ ) in these problems. Unlike the stationary cylinder, rotating cylinder has different kind of nature in physics point of view. Another parameter, spin ratio which is the ratio of tangential velocity at the surface of the cylinder and the stream velocity in uniform flow, gets involved to the entire flow pattern. Rotation of the body induces of the change of the flow direction. Therefore, whole pressure distribution is alternated and become unbalanced. Thus, the lift force is created and the drag force is modified dependent on the configuration. Besides the Reynolds number, spin ratio becomes an essential parameter to control and optimize the aerodynamic forces.

### 1.2.1 Magnus effect

The Magnus effect is known as an unexpected orbit diversion of the objects moving in a flow media with the rotation of their own axis. This effect was first claimed by G.T. Walker in 1671, however, it was mentioned and recognized with the work of G. Magnus [2]. Lafay [3], performed the comprehensive experimental studies in detail. As given in the previous section, the rotation of a body affects the course of the flow,

changing the pressure distribution, causing a force acting on the surface of the body. This force has an opposite sign proportional to the force created by the change of the flow direction. This is called Magnus force. In Figure 1.3, representative image of the Magnus effect is demonstrated.

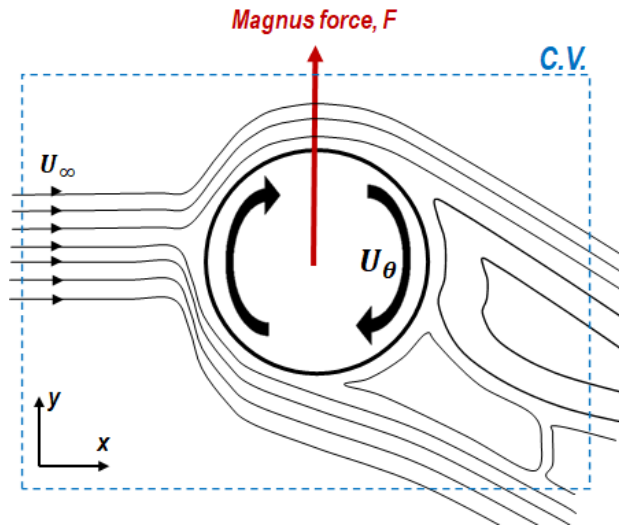


Figure 1.3: Magnus effect

Regarding the Figure 1.3, the flow is induced to move from the left to the right. The upstream of the flow is fully uniform and the  $y$ -velocity is zero at that position. The cylinder, assumed as infinite, has a clockwise rotation, triggering the flow advances downwards. In these conditions, the Magnus force may be defined by using momentum conservation inside the control volume (C.V.) represented in the figure. The basic two-dimensional momentum changes are written as Equation 1.3 and Equation 1.4.

$$F_x = \dot{m}u_{out} - \dot{m}u_{in} \quad (1.3)$$

$$F_y = \dot{m}v_{out} - \dot{m}v_{in} \quad (1.4)$$

$F_x$  and  $F_y$  are the forces which are onset by the convective motion of the flow. The mass flow rate,  $\dot{m}$ , ensuring that the continuity is satisfied inside the control volume.  $u$  and  $v$  represents the  $x$  and  $y$ -velocities, respectively. Sign of these forces are only determined by the velocities entering and exiting from the control volume due to the constant mass flow rate. Concerning the Equation 1.3,  $\dot{m}u_{out}$  and  $\dot{m}u_{in}$  have positive signs, however,  $\dot{m}u_{in}$  is much larger than  $\dot{m}u_{out}$  in magnitude. The resulting force is calculated as in the negative  $x$ -direction, meaning the cylinder intends to go the opposite way to that force. In Equation 1.4, the upstream  $y$ -velocity ( $\dot{m}v_{in}$ ) is zero. In the meantime, there is a  $y$ -velocity in the downstream which is in the course of negative  $y$ -direction. According to the equation,  $F_y$  is obtained as negative, composing the equal and opposite Magnus force.

### 1.2.2 Inverse Magnus effect

Specific conditions are generally connected to specific phenomena in fluid dynamics. The inverse Magnus effect is accepted as one of these unique physical behaviors. Unlike the Magnus effect, the force acting on the cylinder occurs towards directly opposite. The alteration is originated by the restriction of the ranges of Reynolds number ( $99k < Re < 501k$ ) and the low spin ratio ( $\alpha = U_\theta/U_\infty$ ). Outlook of the inverse Magnus effect may be seen with Figure 1.4.

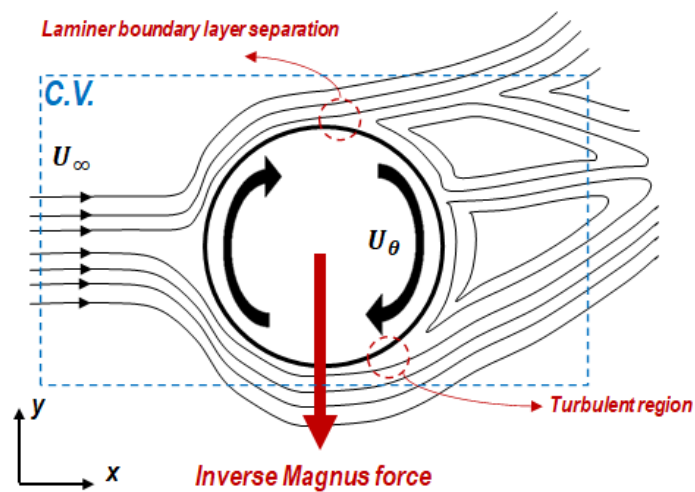


Figure 1.4: Inverse Magnus effect

As a basis, actuation of the inverse Magnus effect is bonded to the characteristics of the separation around the cylinder. In relatively high spin ratio cases which are restricted to a significant range of Reynolds number, retreating (top) side of the cylinder locally possesses low Reynolds number. This actuates the laminar boundary layer separation at this side. However, at the advancing (bottom) side local Reynolds number reaches high values, separating the flow as turbulent. Laminar flow shows substantially weak behavior, resulting with early separation. In contrast, turbulent flow separation is stronger, therefore, flow detaches later. The difference between the locations of separation directs the flow upwards. In addition, turbulent region transfers its momentum and forces the flow upwards as well. Thus, unlike Magnus effect,  $\dot{m}v_{out}$  (Equation 1.4.) is positive, giving the inverse Magnus force towards bottom.



# Chapter 2

## Introduction

As explained in the previous sections, Magnus effect is known as a phenomenon affects the natural projectiles of the spinning objects just as balls used in sports [4,5,6]. Vast number of efforts were given to that scope. Especially, the inversion of the Magnus forces drew the attention among the researchers due to its unforeseen internal.

In 1853, Magnus [2] first reported the deflection of the projectiles of rotating bodies. He tried to explain this interesting behavior with a basic experimental design. Afterwards, Lafay [3] set up an investigation to understand the physics of the Magnus forces and became one of the first researchers observing the inverse Magnus effect. In his work, experimental studies were conducted on rotating cylinder that of without end plates. Various spin ratio and Reynolds number values were considered. Total force around the cylinder were represented for 5 particular Reynolds numbers ( $Re = 62000, 88000, 128000, 168000, 198000$ ). By adjusting the rotation speed of the cylinder, alteration of the spin ratio was provided. In Figure 2.1, the dynamic change of the overall force inclination is given.

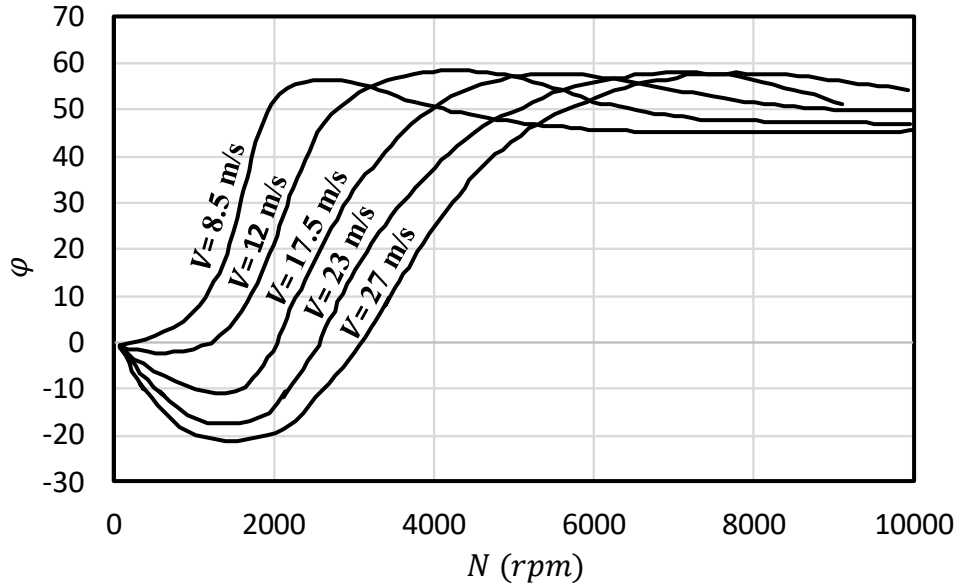


Figure 2.1: Force inclination angle with respect to direction of the stream velocity, reproduced from [3]

In significant spin ratios, he observed the negative force acting on the rotating object. His further research [7] was performed by proving this survey. The objective was to validate the inversion of the Magnus effect by measuring pressure distribution. Cluster of experiments were performed in selected conditions ( $Re = 128000$ ,  $\alpha = 0.21, 0.65, 1.3$ ). It is verified that for the lowest spin ratio, the occurrence of negative forces was repeated. He also clarified that since the pressure is higher at the side in which the tangential velocity of the cylinder and stream velocity own the same direction as the other, the reverse Magnus force appears itself. Later on, Krahn [8] suggested a method for the explanation of the negative Magnus forces. This was the origin of adding the interpretations of transition region to this phenomenon. He proposed a definition called “Effective Reynolds number”. Schematic demonstration of his hypothesis is given in Figure 2.2.

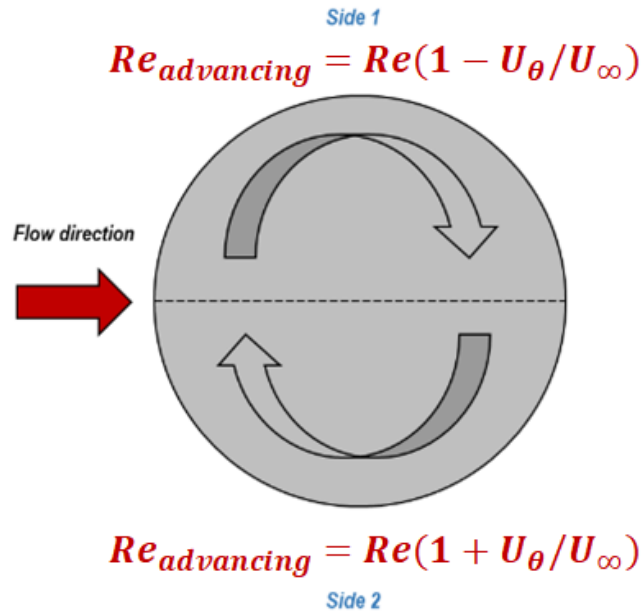


Figure 2.2: Representative image for the Krahn's setup

At the retreating side, effective Reynolds number was defined as  $Re(1 - U_{\theta}/U_{\infty})$ , on the contrary,  $Re(1 + U_{\theta}/U_{\infty})$  on the advancing side. According to his statements, since the  $U_{\infty}$  is much lower than the  $U_{\theta}$ , flow enters the transitional regime at the bottom, contributing fall of pressure and for sure inverse Magnus effect. Enhancing stream velocity induces the increment of effective Reynolds number in the retreating side. Therefore, Magnus effect becomes involved as expected.

A broad-spectrum compilation was executed by Swanson [9] in 1961, including his own experimental work and the former investigations about the Magnus effect. Comparative inferences were performed by the help of the data he collected. The alteration of the lift coefficient with the spin ratio from that work is indicated with Figure 2.3.

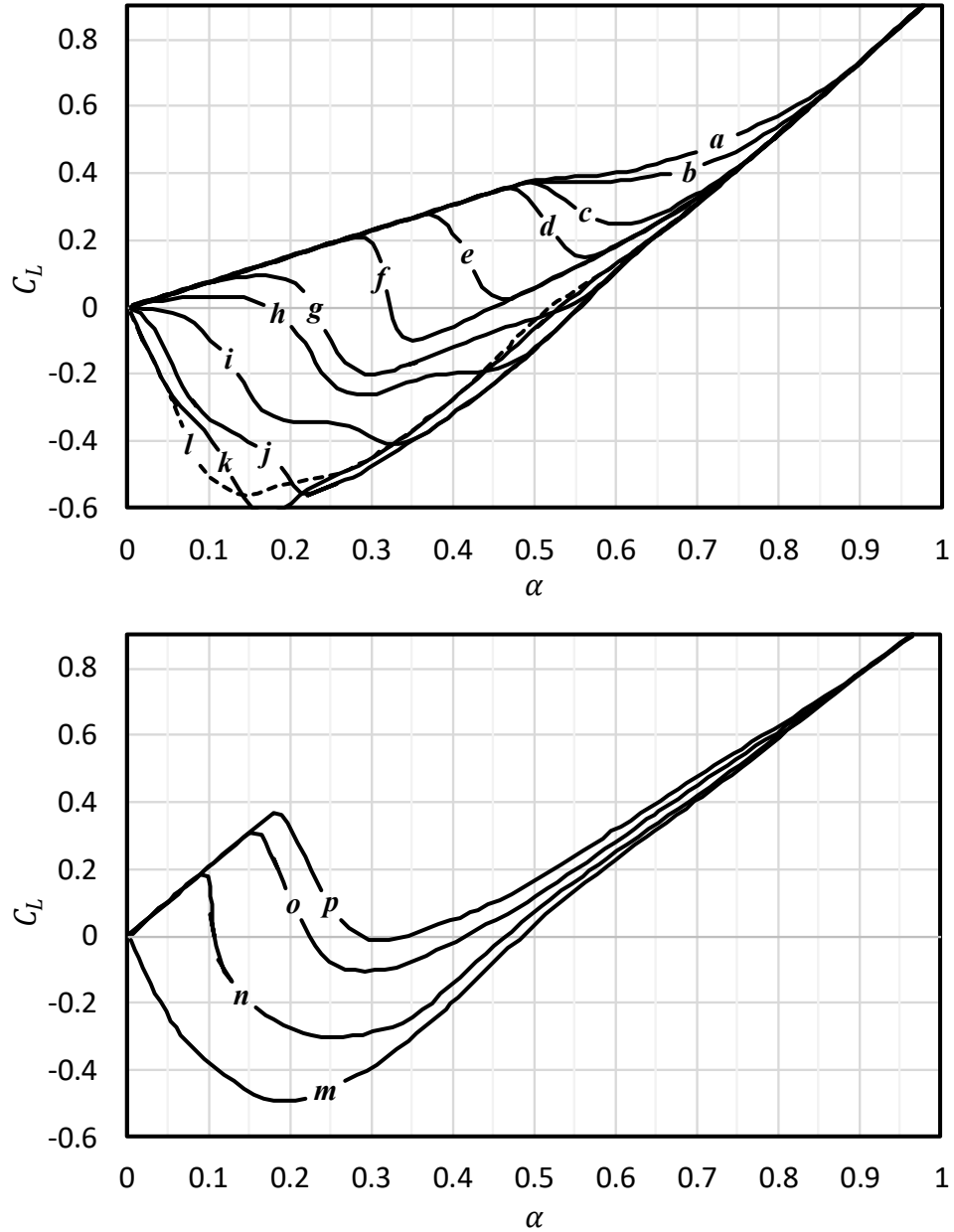


Figure 2.3: Change of lift coefficient with spin ratio, reproduced from [9] (a-f:  $Re = 3.58E+04 - 12.8E+04$ , g-m:  $Re = 15.2E+04 - 36.5E+04$ , n-p:  $Re = 42E+04 - 50.1E+04$ )

In the context of Swanson's work, infinitely long cylinder geometry was assumed and extensive ranges of the Reynolds number ( $36000 < Re < 501000$ ) and spin ratio ( $0 < U_\theta/U_\infty < 1$ ) were considered. As a result of the study, it is seen that the negative Magnus effect was only encountered in at least  $Re = 99000$  and at most  $Re = 501000$ .

One of the early examples of numerical investigation of the inverse Magnus effect was conducted by Fletcher [10]. By developing potential flow model, it was aimed to estimate the forces on a rotating ogive cylinder. All calculations were achieved at a subcritical Reynolds number and low spin ratio. Acceptable match was obtained regarding the past experiments. Interpretation has always covered a high percentage of the cross-flow problems of rotating cylinders. Concerning the explication of Magnus forces is accepted as one of the most compelling features of these flows [9]. Maruyama [11] discussed two different approaches to explain the physical mechanism behind the Magnus effect. Priorly, Bernoulli's theorem was taken into account, not providing a correct point of view, due to its strong explanatory nature in inviscid regions. However, the second way was far sensible which using the span occurring between the separation points at two sides.

Another numerical investigation was completed on a rotating sphere by Muto et al. [12]. In this study, they utilized large eddy simulation (LES) with the dynamic sub-grid model. Three separate flow regimes (subcritical, critical and supercritical) were considered, supplying negative Magnus force only in the critical flow regime. Researchers attributed this physical manner in terms of the type of flow separation. Same year, Kray et al. [13] experimentally investigated the flow field and aerodynamic forces on a rotating sphere. Flow visualization was achieved by aerosol injection to the wake region and oil film technique. Force measurements were done by using six-component force balance. In a wide range of Reynolds number and spin ratio, negative Magnus effects were reached. Additionally, with the alteration of conditions, variation of the wake structures was visualized.

Recently, turbulence models have been on trial for predicting reverse Magnus forces. One of these studies was performed by Kusyumov et al. [14], considering the laminar to turbulent transition phenomena with  $k-k_l-\omega$  transition model. Capturing negative forces were accomplished. It was shown that transition to turbulence and inverse Magnus effect are directly associated. Although the promising results were reported, certain differences with experimental references were acquired. Zheng et al. [15] suggests two-dimensional coupled model which contains  $\gamma-Re_\theta$  and SST  $k-\omega$  models. They claimed that the model calculated the inverse Magnus effect well. As following, one experimental design was carried out by Kim et al [16], including rotating sphere,

using digital particle image velocimetry (DPIV) so as to observe the flow field. In order to estimate the location of the flow separation, empirical formulation was proposed by the help of lift and drag calculations. The point where the lift coefficient has a sudden decrease with increasing spin ratio is called lift crisis. Cheng et al. [17] remarked this behavior in their study. Cases of fixed Reynolds number accompanying various spin parameters were examined. Results were compared to the past studies [9, 18, 19, 20]. Nguyen et al. [21] investigated the influence of the shape of the spinning bodies and their surface roughness. They attempted to test different geometries, such as cube, ellipsoid, sphere, cylinder etc. In these particular geometries, change of the lift coefficient was pursued for the smooth and rough surfaces. For the sphere and ellipsoid, it is represented that negative Magnus effect (lift crisis) arises for given Reynolds number. All issued papers were done for understanding the flow physics and the mechanism behind this special phenomenon.

In this study, a cylinder that has partially actuated moving surfaces [22] is numerically investigated. The goal is that reaching the ordinary and inverse Magnus forces by optimizing the actuator configuration to control circulation around the cylinder. In order to achieve this, two-dimensional numerical model was generated in company with  $k\text{-kl-}\omega$  turbulence model. By virtue of there is lack of distinct methodology for detecting the separation point around moving walls (especially at upstream-moving wall) and the laminar to turbulent transition station, two novel methods were developed for determining separation and transition locations. By means of these criteria, relationship between the separation, the transition and the Magnus phenomenon were clarified delicately. It is predicted that the current study will be a guide with its important outputs in the use of the Magnus effect, particularly inverse Magnus effect, on controlling lift and drag forces acting on aircrafts, as well as the methodology of separation criteria which is compelling for the rotating cylinders.

# Chapter 3

## Numerical Method

In this chapter, computational details of the present study were discussed. Determination of the numerical strategy was given, and the validation study was elaborately clarified.

### 3.1 Selection of Method

As mentioned, large number of numerical studies have been performed to investigate the Magnus phenomena in the past. However, only a few of them provided success for observing the inverse Magnus effect. The reason is that evolution of the negative Magnus forces is completely attached to the transition to turbulence characteristics of the flow, and numerical models must have a feature of capturing the transition and turbulence. Following sub-sections represent the background of some numerical models and their usage in Magnus effect.

#### 3.1.1 Large eddy simulation (LES)

Turbulence is a fully observable feature of the flow. Numerical solution of Navier-Stokes equations makes possible to be observed the all the turbulent scales, only if the entire scales of time and space are resolved. Direct numerical simulation provides feasibility to that purpose [23]. Unfortunately, DNS has an expensive computational cost at the high Reynolds numbers considered in this study, on the order of  $10^{-5}$  to  $10^{-6}$ , preventing to be used on complex and practical problems and optimizations. This drawback was tried to be surpassed by researchers proposing a new method named Large eddy simulation (LES). LES is a mathematical model to conduct simulations of turbulent flows, more cost-effective than DNS by deactivating the solution of small

scales of turbulent structures. Low-pass filtering is implemented on Navier-Stokes equations; thus, only large scales which are dominantly contributing to the energy and momentum transfer, are computed. Small scales are considered by sub-grid scale models. Filtered LES equations shows resemblance to the well-known Reynolds averaged Navier-Stokes (RANS) equations; therefore, it may be seen that LES is a way of combination of unsteady RANS and DNS [23, 24].

Turbulence initiates from the wall. Eddy sizes are small where the momentum transfer is driven by viscosity in  $0 < y^+ < 40$  [25]. For the cases that includes investigation of near the wall region is prior, models predicting the behavior of this particular layer of flow is necessary. Hence, in current problem, LES considered as an option regarding the modeling capabilities of small eddies and transition phenomenon. While LES is quite useful for the problems containing essential aims and basic geometries, for the optimization cases it may not be categorized as a practical tool. In the vicinity of the walls, LES requires fine grid with a sufficient aspect ratio of each element. In order to capture eddies,  $y^+$  should be less than 1, while  $x^+$  and  $z^+$  is less than 10. It is necessary to get low aspect ratio rectangular elements as far as possible which is not required in RANS simulations. Besides that, three-dimensional model generation is a necessity needing the large number of spatial discretized elements which has the potential of long computation time. Due to those specifications of the LES, it was not found compatible with the present study.

### 3.1.2 $\gamma - Re_\theta$ model (Transition – SST model)

The transition  $\gamma-Re_\theta$  model is *SST*  $k-\omega$  based turbulence model was first proposed by Menter and Langtry [26] including additional two transport equations to detect the transition phenomenon. These two transport equations are intermittency and transition onset criteria equations as a function of momentum thickness Reynolds number. Other transport equations are standard *SST*  $k-\omega$  equations, such as turbulent kinetic energy and specific dissipation rate. Considering the features of the model, it was chosen as one of the candidates to carry the recent study forward.



### 3.1.3 Transition $k\text{-}kl\text{-}\omega$ model

Another RANS based turbulence model is  $k\text{-}kl\text{-}\omega$  transition model [27]. This model was generated to predict the bypass and natural transition scenarios. As another  $k\text{-}\omega$  based model, it includes three transport equations. The turbulent kinetic energy equation is the main equation for this model, having supplemental expressions which are laminar kinetic energy equation and specific dissipation rate. Due to its potential for predicting transition,  $k\text{-}kl\text{-}\omega$  turbulence model was selected as second model to observe inverse Magnus effect.

## 3.2 Computational domain

Numerical details are given as from this section. Three models that are explained earlier must be tested for their reliability. For that purpose, two-dimensional unsteady numerical model was generated. In Figure 3.1, the computational flow domain is presented. The domain is created in ANSYS Design Modeler and it is planned to be made sufficiently wide to eliminate the wall effects.

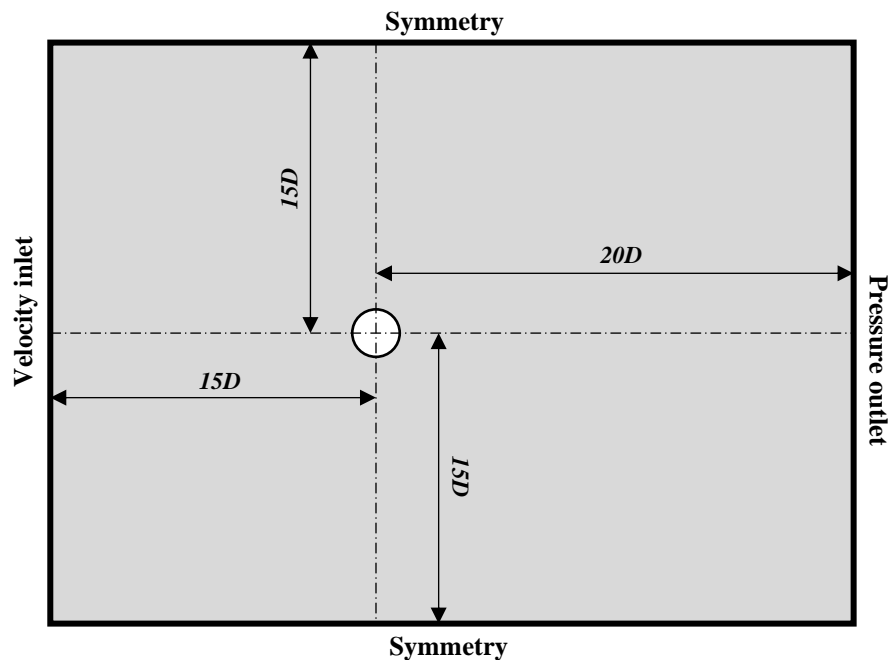


Figure 3.1: Computational domain

Cylinder diameter is  $D = 0.04$  m, proportionally, domain sizes are  $15D$  for each vertical height with respect to streamwise direction. Starting from upstream, the length through center point of the cylinder was defined as  $15D$ . Up to downstream, the streamwise span is  $20D$ . A depth is implied as a reference in order to obtain proper lift and drag evaluations.

### 3.3 Grid structure

Aiming the optimized computational solutions, steady-state mesh dependency analyses were conducted for stationary cylinder. Working fluid was chosen as water. Simulations were carried out at  $Re = 128000$ . The combination of tri and quad meshes were generated, preferring curvilinear quad grid in the vicinity of the cylinder, unstructured tri mesh at the far fields. At four different grid resolutions (58k, 70k, 168k, 235k elements) lift and drag coefficients were compared. Table 3.1 indicates each difference percentage of three cases regarding the grid-independent finest grid (235k) and the explanation of error calculation.

Table 3.1: Convergence of each mesh compared to the maximum resolution (235k elements)

Number of Elements	$0.58 \times 10^5$	$0.7 \times 10^5$	$1.68 \times 10^5$
$*(e_{C_L})_s$	0.6	0.2	0.2
$(e_{C_D})_s$	1.4	0.3	0.3

$$*(e_{C_L})_s = \frac{|(\overline{C_L})_{2.35 \times 10^5} - (\overline{C_L})_i|}{|(\overline{C_L})_{2.35 \times 10^5}|} \times 100, i: 0.58 \times 10^5, 0.7 \times 10^5, 1.68 \times 10^5$$

$(e_{C_L})_s$  and  $(e_{C_D})_s$  represents the spatial error between the sample cases and the best resolution. Error calculations were done by using averaged quantities,  $\overline{C_L}$  and  $\overline{C_D}$ . After the grid dependency study, mesh with 70k elements was found sufficient. The structure includes 550 divisions in circumferential direction with maximum skewness of 0.72. First layer thickness was considered by satisfying  $y^+ < 1$ . The computational grid is demonstrated in Figure 3.2.

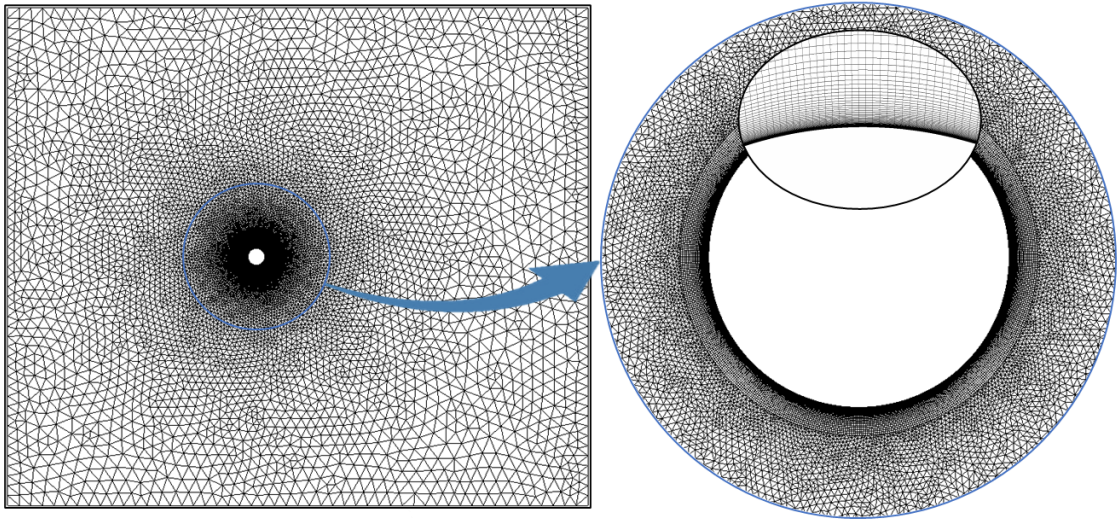


Figure 3.2: Mesh structure

### 3.4 Solution method

Inverse Magnus effect is excessively dependent on the turbulent structures. Therefore, fully turbulent simulations are needed to be conducted. Besides that, laminar flow analyzes are executed to validate the model. Validation study will be given in the further chapters.

As mentioned in the previous sections Reynolds averaged Navier-Stokes (RANS) based turbulence models are determined the most convenient approaches to the motivation and nature of recent investigation. Turbulence was modeled with two different methods, choosing one of them provided continuation of the study after its verification. Ansys FLUENT was chosen as a software for the simulations. Further adjustments were made on the selected software. In order to solve the problem, the implicit SIMPLEC algorithm was used for pressure-velocity coupling. The PRESTO scheme was utilized for the discretization of the pressure. This is unstructured mesh variant of the staggered grid arrangement for structured grids as discussed by Patankar [28] as well as Versteeg and Malalasekera [29] and enables better pressure-velocity coupling. The second order upwind scheme was applied for the convective terms. The first order implicit scheme (implicit Euler method) was used for time-marching. Continuity and momentum equations were solved, corresponding appropriate temporal

and spatial resolutions. Transient results were obtained at each time step and average quantities of variables were used.

### 3.5 Boundary and initial conditions

Top and bottom boundaries are given as symmetry boundary condition. Hence, wall effects are minimized in possible sources. Left boundary is applied inlet which the turbulent intensity ( $I$ ), is defined as 0.5% where the uniform velocity distribution is employed. At the right, atmospheric pressure is determined. The surface of the cylinder set as the no-slip wall boundary. The cylinder wall is altered regarding the type of the cases as rotating or stationary. The working fluid is defined as water in order to compare the results of future experimental work without analogy. In Table 3.2, physical properties of water are represented.

Table 3.2: Physical properties of water at 25°C, 1 atm

Material	Density	Dynamic Viscosity
	$\rho$ (kg/m <sup>3</sup> )	$\mu$ (kg/m.s)
Water	997.05	8.9E-4

Water is initially stagnant inside the domain. The movement of the water triggered by the inlet stream velocity. At the start turbulent intensity is zero except the inlet.

### 3.6 Temporal resolution analysis

Optimum temporal resolution is a key of obtaining confidential outputs. The pre-defined configuration of stationary cylinder flow simulation was repeated in transient conditions. Laminar, two-dimensional model was tested by using 7 different Courant numbers at  $Re = 128000$ . The definition of the local Courant number [23] was given with Equation 3.1.

$$Co = U_i \frac{\Delta t}{\Delta x_i} \quad (3.1)$$

In the equation,  $U_\infty$  represents the stream velocity,  $\Delta t$  is the time step and  $\Delta x$  is the interval of the length of the smallest mesh. The Courant number was fixed at various points and the values of the time step were calculated. In the beginning, the stability of the vortex shedding was reached with  $Co = 10$ . Afterwards, various Courant numbers was utilized for the continuation of the analysis after the stabilization (Duration is 0.5s.). The results of the time-dependency study were given by Table 3.3.

Table 3.3: Time resolution convergence by the lowest Courant number case ( $Co = 0.1$ )

$Co$	0.1	0.25	0.5	1	2	5	10
$*(e_{C_L})_t$	0	0.4	0.5	2.5	5.8	9.9	97
$\sigma_{C_L}$	1.1	1.1	1.1	1.1	1.1	1.1	1.1
$(e_{C_D})_t$	0	0.6	1.9	0.4	1.1	1.4	4
$\sigma_{C_L}$	0.2	0.1	0.1	0.1	0.1	0.1	0.1

$$*(e_{C_L})_t = \frac{|(\overline{C_L})_{Co=0.1} - (\overline{C_L})_{Co}|}{|(\overline{C_L})_{Co=0.1}|} \times 100, Co = 0.25, 0.5, 1, 2, 5, 10$$

As a finest time discretization,  $Co = 0.1$  was chosen, due to after which supplies the independence from time. Each case was compared by the average drag and lift coefficients regarding the finest Courant results, percentages of the error were indicated.  $(e_{C_L})_t$  and  $(e_{C_D})_t$  indicates the temporal error between the sample cases and the best resolution. Error calculations were done by using time-averaged quantities,  $\overline{C_L}$  and  $\overline{C_D}$ . The standard deviation values were also given in Table 3.3. In the current study, time cost of the simulations is also a factor that must be considered besides the accuracy. While case  $Co = 0.1$  lasted 1 week,  $Co = 5$  case ended in only 20 hours. The target error was set less than 10% which is sufficient for the nature of the current study. Therefore,  $Co = 5$  was accepted as the best approach which meets the requirements of time consumption and the precision of the simulations. The non-dimensional time step was defined as shown in Equation 3.2.

$$\Delta t^* = U_\infty \frac{\Delta t}{D} \quad (3.2)$$

$\Delta t^*$ ,  $U_\infty$ ,  $\Delta t$  and  $D$  represent the non-dimensional time step, the flow stream velocity, time step and the diameter of the cylinder, respectively. At  $Co = 5$ , the goal of  $\Delta t^* \leq 0.01$  was reached [15]. The dimensionless flow time ( $t^*$ ) was specified as 250 for evaluating trustable statistics.

## 3.7 Validation

The validation study involves two stages to check the reliability of URANS simulations with two different turbulence models claimed to be successful predicting the inverse Magnus effect. The verification process was carried out by checking the stationary cylinder, followingly, rotating cylinder.

### 3.7.1 Stationary cylinder

Stationary cylinder was investigated by the light of the study of Rosetti et al. [24] was considered. They assessed the convenience of the  $k-\omega$  SST turbulence model for flow around circular cylinder, in terms of aerodynamic forces, flow separation points and Strouhal number.

Current simulations are conducted by  $\gamma-Re_\theta$  (transition-SST) and  $k-kl-\omega$  transition models for four different Reynolds numbers (100, 10000, 100000, 500000) in laminar and turbulent flow regimes. In Figure 3.3a, drag coefficients are compared with a set of experiments and URANS model of Rosetti's study.

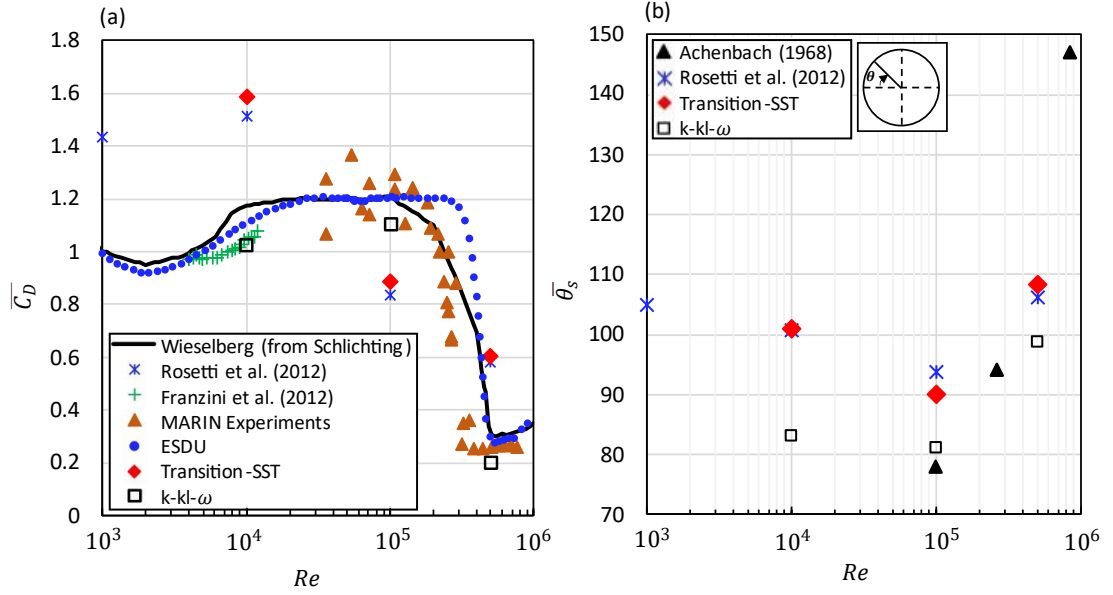


Figure 3.3: (a) Change of the time-averaged drag coefficient with respect to Reynolds number. (b) Variation of the time-averaged separation angle results.

[1,24,25,30,31,32,33]

The  $\gamma-Re_\theta$  transition model indicated rather similar results to the Rosetti's  $k-\omega$  SST model, as a result of its foundation of being  $k-\omega$  based model. However, the  $k-kl-\omega$  model showed that there is a better agreement than  $\gamma-Re_\theta$  regarding the values of drag coefficient in experimental studies for both subcritical and critical regimes. The level of accuracy of this model was observed that more than sufficient compared the other URANS simulations combined with turbulence models. Figure 3.3b indicates the separation points at the top side of the cylinder. In laminar condition, flow separates closer to the downstream stagnation point than the turbulent states. The dynamic characteristic of turbulent flow causes the instabilities [24], such that, flow separates earlier. In this study, similarity with the experimental data is the most crucial factor for the following work. According to the Figure 3.3b, one is able to say that the  $k-kl-\omega$  transition model successfully predicts the separation points. In order to examine the performance of  $k-kl-\omega$  profoundly, skin friction coefficients in the vicinity of the cylinder were compared in Figure 3.4 with Achenbach's experimental investigation [33].

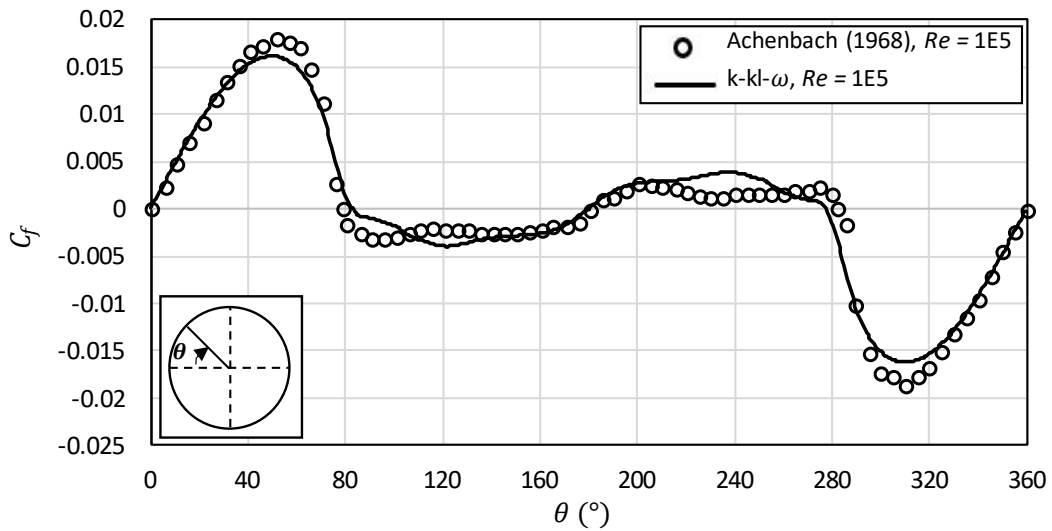


Figure 3.4: Skin friction coefficients around the cylinder [33]

In given Reynolds number, once again,  $k-kl-\omega$  turbulence model represented an excellent agreement in flow behavior, trend of skin friction coefficients and separation angles. The agreement in skin friction coefficients provides a double assurance to the drag and separation results.

### 3.7.2 Rotating cylinder

Two-dimensional flow simulations were continued with rotating cylinder geometry. Analyses were carried out in one of the critical Reynolds numbers (128000) from Swanson's study [9] and various spin ratios. Swanson observed a negative Magnus force in not only similar conditions but also in a comprehensive experimental study. For further developments, the results of this study were chosen as a verification point of view. URANS modeling with different turbulence models were considered. Inlet stream velocity calculated by the parameters of water and Reynolds number ( $U_\infty = 2.856$  m/s). In Figure 3.5, lift and drag coefficients for several models and spin ratio are represented.



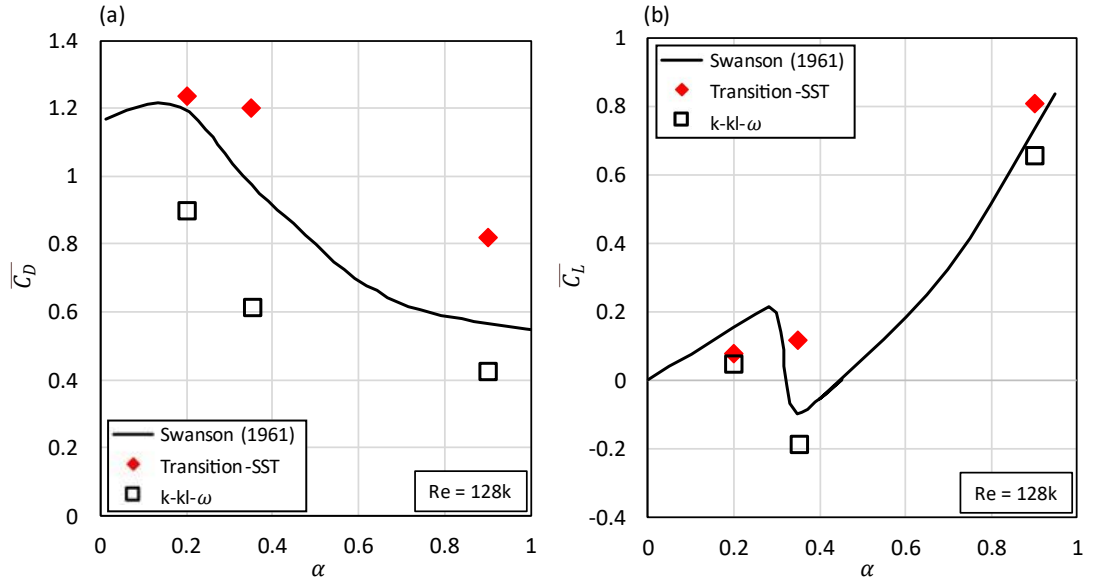


Figure 3.5: Validation study for fully rotating cylinder at constant  $Re = 128k$ . Time-averaged lift ( $\overline{C_L}$ ) and drag ( $\overline{C_D}$ ) coefficients are indicated with spin ratio ( $\alpha$ ) for *Transition-SST* and *k-kl- $\omega$*  turbulence models. [9]

Simulations were performed with two particular models, such as, *Transition-SST* and *k-kl- $\omega$* . Simultaneously, three different spin ratio values were taken into account (0.2, 0.35 and 0.9). In accordance with the benchmarking of the current results and experiments, except for *k-kl- $\omega$*  transition model, capturing the negative lift coefficient have been resulted an inefficacy in URANS models (on the contrary of Zheng et al. [15]). As seen in Fig. 3.6, drag and lift coefficients has a consistent trend with regards to experimental study of Swanson [9] with *k-kl- $\omega$*  transition model. Principally, at  $\alpha = 0.35$  which is expected condition of the negative lift forces, it featly predicted the flow physics of inverse Magnus effect. It was proved that the model provided an opportunity to observe inverse Magnus forces.

# Chapter 4

## Results

In this chapter, the interpretation of conventional and novel approaches to the Magnus effect were executed by developing newly introduced post-processing tools. Later on, the optimization study was represented on a novel geometrical design.

### 4.1 Development of transition onset and separation point criteria for arbitrary circulation distribution

The explanation of a negative Magnus lift is come up with a variety of flow and turbulence properties such that some clarifications were given by Swanson [9] and Fletcher [10]. The most popular statement is related to the position of the separation at two sides of a cylinder. These are called as advancing side ( $0^\circ < \theta < 180^\circ$ ) and receding side ( $180^\circ < \theta < 360^\circ$ ). In order to observe the negative lift values, the fundamental condition must be a beforehand flow separation at receding side.

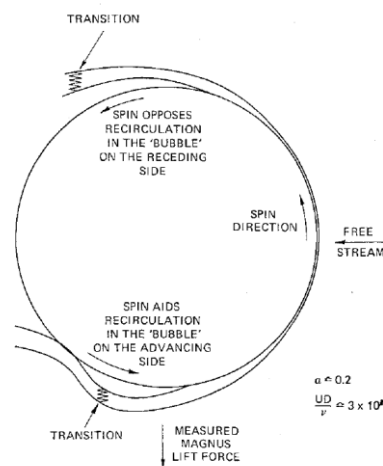


Figure 4.1: Appropriate conditions for inverse Magnus effect [10]

Typically, the transition onset angle takes place as a second provision to access negative lift characteristic. At receding side, it is expected that there occurs a laminar boundary layer separation, contrarily, at advancing side a turbulent boundary layer separation is an obligation. Consequently, at the top region, flow separates weaker and earlier. However, turbulent structures of bottom region strongly transport momentum and force the flow upwards. In the critical Reynolds number region, presence of a separation bubble in boundary layer at two sides, specifies the type of Magnus forces (see Figure 4.1). Normally, positive forces are reached in non-critical Reynolds number. Spinning delays the separation point throughout the stagnation area located downstream of the cylinder. However, at the critical Reynolds number, flow transition onsets far beyond from the separation. In other words, locally, the Reynolds number decreases drastically, so that, flow separates in laminar regime. At the advancing side, rotational movement of the body helps to the recirculation at that region. Separation bubble is occupied, and local Reynolds number is dramatically increased. As a result, transition starts before the separation. Turbulent boundary layer separation is observed. The upwards movement of flow creates a force which has a reverse direction.

Predicting the separation points and the onset locations of transition are fairly substantial, providing an access to carry out these given expositions.

#### 4.1.1 Transition criterion

Turbulence occurs by the cause of instabilities in flows that are realized at high Reynolds numbers [34]. The transition is a characteristic of flow, held in between laminar and turbulent flow regions, enabling the flow becomes turbulent. The onset of the turbulence is found by checking the starting position of transitional region. Regarding the current study, if the separation location is known, the transition process from laminar to turbulent flow enables the information about the behavior of the flow separation. This opens a way to the interpretation of the Magnus effect.

In order to generate a transition criterion, some basic variables such as, turbulence intensity and turbulent viscosity, were considered. Sudden increase in these two variables demonstrates that the turbulence arises on the location observed, having a unity of them can give a reliable onset location. Turbulence intensity essentially indicates the level of turbulence in flows. This feature comes from real physical

behavior of the velocity fluctuations [34]. The formulation of turbulence intensity [35] was given by Equation 4.1.

$$I = \frac{u'}{U} \quad (4.1)$$

where  $u'$  is the root mean square of the turbulent velocity fluctuations and  $U$  is the reference velocity at each particular position.

$$u' = \sqrt{\frac{1}{3}(u'_x{}^2 + u'_y{}^2 + u'_z{}^2)} = \sqrt{\frac{2}{3}k} \quad (4.2)$$

The velocity fluctuation term can be written as a function of turbulent kinetic energy ( $k$ ) as seen in Equation 4.2. Combination of Equations 4.1 and 4.2. gives another expression to define turbulence intensity in Equation 4.3.

$$I = \frac{\left(\frac{2}{3}k\right)^{\frac{1}{2}}}{U} \quad (4.3)$$

Another element of the criterion is turbulent viscosity, which is used for creating artificial turbulence condition by adding it to the dynamic viscosity of the fluid. In  $k$ - $\omega$  based models, turbulent viscosity is calculated by using specific dissipation rate ( $\omega$ ) and turbulent kinetic energy ( $k$ ). Equation 4.4 and Equation 4.5 represent the definitions of turbulent viscosity and specific dissipation rate [35].

$$\mu_t = \frac{\rho k}{\omega} \quad (4.4)$$

$$\omega = \frac{k^{\frac{1}{2}}}{(C_\mu)^{\frac{1}{4}} l} \quad (4.5)$$

$\mu_t$  corresponds the turbulent viscosity,  $\rho$  gives the constant density in incompressible flow,  $C_\mu$  is the model constant in the  $k$ - $\omega$  based models and  $l$  is the turbulent length scale. When these equations are combined with each other, the turbulent viscosity can be found as following in Equation 4.6:

$$\mu_t = \frac{\rho k (C_\mu)^{\frac{1}{4}} l}{k^{\frac{1}{2}}} \quad (4.6)$$

Reaching the non-dimensional form was determined as the main purpose on this criterion. Therefore, turbulence intensity is divided to the turbulent viscosity as a first step. Equation 4.7. shows the structure of this ratio.

$$\frac{I}{\mu_t} = \frac{0.667}{U \rho (C_\mu)^{\frac{1}{4}} l} \quad (4.7)$$

Due to the flow is incompressible,  $\rho$  assumed as constant.  $U$  represents the reference velocity, which is also constant for each position. However, all three of variables such as, the turbulent length scale ( $l$ ), reference velocity and density were determined as dimensional in the Equation 4.7. The expression was become non-dimensional by combining it with the wall normal distance corresponding different  $y^+$  values, free-

stream velocity and reference density. The reason is that  $I$  and  $\mu_t$  were obtained from a broad range of radial positions, eliminating non-consistent output to reach the best possible result. The non-dimensional form of the Equation 4.7. was introduced by the Equation 4.8.

$$\frac{I}{\mu_t} y = \frac{0.667}{U \rho (C_\mu)^{\frac{1}{4}} l} y \rho_{ref} U_\infty \quad (4.8)$$

Normalization process was implemented on the equation by taking the hyperbolic tangent of the expression. Afterwards, the integration throughout the cylinder was executed at each side individually. In order to evaluate the point at which the sudden change is observable, the second derivative of the final values was taken with respect to  $\theta$ . Whole process is defined in terms of single parameter,  $C_t$ . Inflection point gave the transition onset location. In Equation 4.9., whole process was indicated as a mathematical expression.

$$\frac{d}{d\theta} \left( \frac{d}{d\theta} (C_t(\theta_{tr})) \right) = \frac{d}{d\theta} \left( \frac{d}{d\theta} \left\{ \left[ \tanh \left( \frac{I(\theta_{tr})}{\mu_t(\theta_{tr})} y \rho_{ref} U_\infty \right) \right]_{y^+=value} \right\} \right) = 0, \quad (4.9)$$

$$0 \leq \theta \leq 180,$$

$C_t$  represents the transition criterion. Equation 4.9 was used with various  $y^+$  values. As a test case, generic stationary cylinder was chosen in condition of subcritical  $Re = 10^5$ . The transition onset angles for different  $y^+$  values were provided in Figure 4.2.

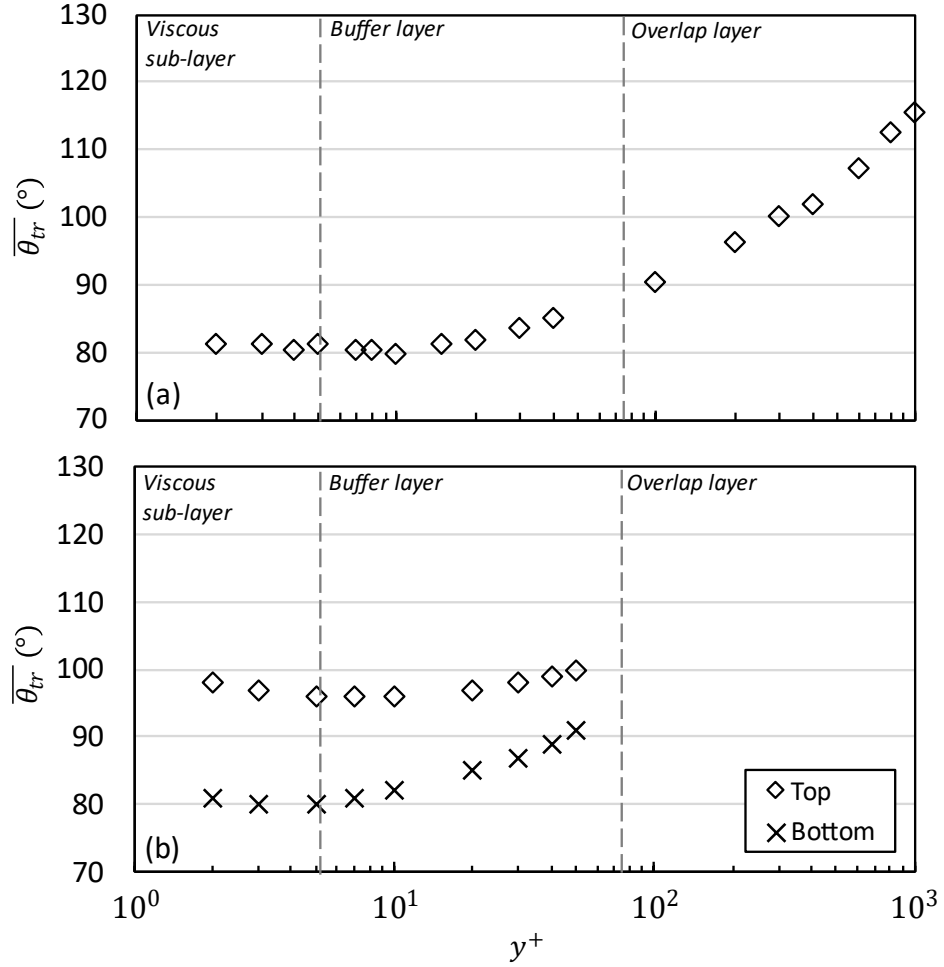


Figure 4.2: Transition onset angles calculated by the current criteria calculated by time-averaged turbulence properties,  $\overline{\theta_{tr}}$ , with respect to  $y^+$ . (a) Stationary cylinder, (b) fully rotating cylinder

Figure 4.2a shows that transition angles indicated strongly consistent trend in the range of  $2 < y^+ < 15$ . After  $y^+ = 15$ ,  $\overline{\theta_{tr}}$  starts to increase and this increment behavior constantly continues in the farther  $y^+$  values as well. As a well-known feature of boundary layer structure, in the viscous sub-layer ( $y^+ < 5$  [1]), flow is driven only by viscosity and the turbulence effects are no longer exists in this region. However, the transition to turbulence commences to occur in the early position of the buffer layer ( $5 < y^+ < 70$  [1]) [36]. Thus,  $y^+ = 5$  was chosen as the reference radial position to obtain the turbulence properties. As a result of the onset criterion  $\overline{\theta_{tr}}$  is found as  $80.43^\circ \approx 80^\circ$ . Figure 4.2b, the transition angles are obtained for the fully rotating cylinder ( $\alpha =$

0.35). The same consistency is observed around the  $y^+ = 5$ , although the characteristics of the top and bottom transition are different. This supports the argument of radial location selection given for the stationary case.

## 4.1.2 Separation criterion

Finding the flow separation locus is of capital importance to the current study which the explanation of Magnus effect depends upon the differences of separation points at both advancing and receding sides. Fundamentally, the separation location in two-dimensional steady flows is defined by the zero shear stress or skin friction:

$$\tau_w = \mu \left( \frac{\partial u}{\partial n} \right)_w = 0 \quad (4.10)$$

That means there is no longer velocity change in the normal direction inside the boundary layer. Adverse pressure gradient takes the control after the location which has zero velocity gradient. On the contrary, when the boundary layer separation occurs on a moving surface, zero shear stress does not necessarily indicate where the separation is constituted [37]. According to the relative motion of the wall surface regarding the flow direction, determining the exact separation location becomes a complicated issue. In order to solve this problem, another criterion was separately offered by Moore [38], Rott [39] and Sears [40]. After these publications, the criterion was started to be called “MRS criterion”, which is shown in Equation 4.11.

$$\tau_w = \mu \left( \frac{\partial u}{\partial n} \right)_w = 0, u = 0 \quad (4.11)$$

Besides the zero skin friction, streamwise velocity component must be zero to ensure separation. In Figure 4.3, the mechanism of the MRS criterion was given.



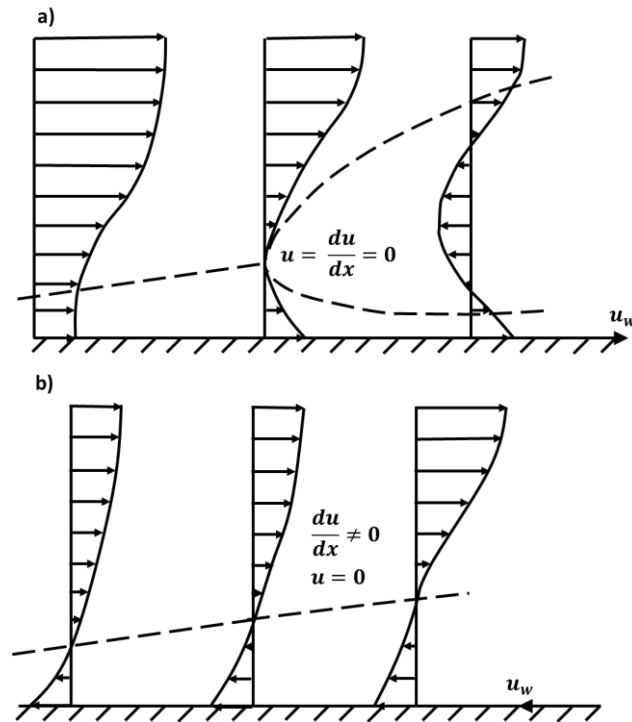


Figure 4.3: Demonstration of flow over moving walls at, (a) downstream-moving wall, (b) upstream-moving wall [41]

In the downstream moving wall where the wall movement is in the streamwise flow direction, the separation is not observed near the wall region. Despite the velocity gradient is zero in some significant locations, that does not signify the separation due to the favorable pressure gradient. As the MRS criterion satisfies, adverse pressure gradient appears itself among the far field and the vicinity of the wall. A set of experiments were achieved in the past studies (Sears and Telionis [42], Koromilas and Telionis [41], Ludwig [43]), verifying the effectiveness of the MRS criterion.

In contrast to the MRS criterion has a certain success to predict the separation points at the downstream moving walls, it is never satisfied for the upstream moving walls (Inoue [44], O'Brien [45], Peller [46], Degani et al. [47], Yapalparvi and Van Dommelen [48]). The wall moves exactly opposite direction with respect to the flow, causing the existence of zero velocity line where the inflection point of the velocity vectors. This sudden change in the sign of velocity vectors confirms that the gradient of the velocity is always different from zero in  $u = 0$  locations. Therefore, the curves of  $\partial u / \partial n = 0$  and  $u = 0$  cannot intersect each other.

In order to solve this problem, a novel methodology for a rotating cylinder is proposed for the estimation of separation in both downstream (top side) and upstream (bottom side) moving walls. The method was impressed by the book of Belotserkovsky et al. [35] which includes a different perspective of separation prediction process by using the combination of pressure distribution, momentum thickness ( $\delta^{**}$ ), and displacement thickness Reynolds number. Pressure distribution was chosen as a variable due to its characterization of when the separation occurs, there is no gradient in circumferential direction. In this way, the separation can be predicted not as a point, but a region. Alternatively, the displacement thickness ( $\delta^*$ ) is another appropriate element that can be embedded inside a criterion. The benefit to choose it as a variable is to interpret the data both physical and mechanical sense. In consequence, gradients of the displacement thickness and pressure with respect to angular position were used to constitute a separation criterion. Additionally, Reynolds number was modified by the displacement thickness and the velocity at the far field in the domain. The formulation of the modified Reynolds number was represented in Equation 4.12 and Equation 4.13.

$$Re^* = \frac{\rho(U_\infty - U_\theta)\delta^*}{\mu} \quad (\text{downstream moving wall}) \quad (4.12)$$

$$Re^* = \frac{\rho(U_\infty + U_\theta)\delta^*}{\mu} \quad (\text{upstream moving wall}) \quad (4.13)$$

where  $U_\infty$  and  $U_\theta$  represent free stream velocity and tangential velocity, respectively. At  $Re = 128000$ , stationary cylinder and three ( $\alpha = 0.2$ ,  $\alpha = 0.35$ ,  $\alpha = 0.9$ ) different rotating cylinder cases were examined by implementing set of different criteria. In regard of MRS criterion, the separation angles at the top side of the cylinder ( $(\overline{\theta}_s)_t$ ) were found which were used for the verification of the recent criterion. Table 4.1. provides this separation angles.

Table 4.1: Separation angles,  $(\overline{\theta}_s)_t$  found by MRS criterion at stationary and fully rotating cases on the top side of the cylinder

Cases	$\alpha = 0$	$\alpha = 0.2$	$\alpha = 0.35$	$\alpha = 0.9$
$(\overline{\theta}_s)_t$ ( $^\circ$ )	82	92	96	119

Initially, gradients of the displacement thickness and the pressure coefficient values regarding  $\theta$  were calculated to obtain the raw behavior of these variables by plotting them against the error of  $\theta$  as seen in Figure 4.4.

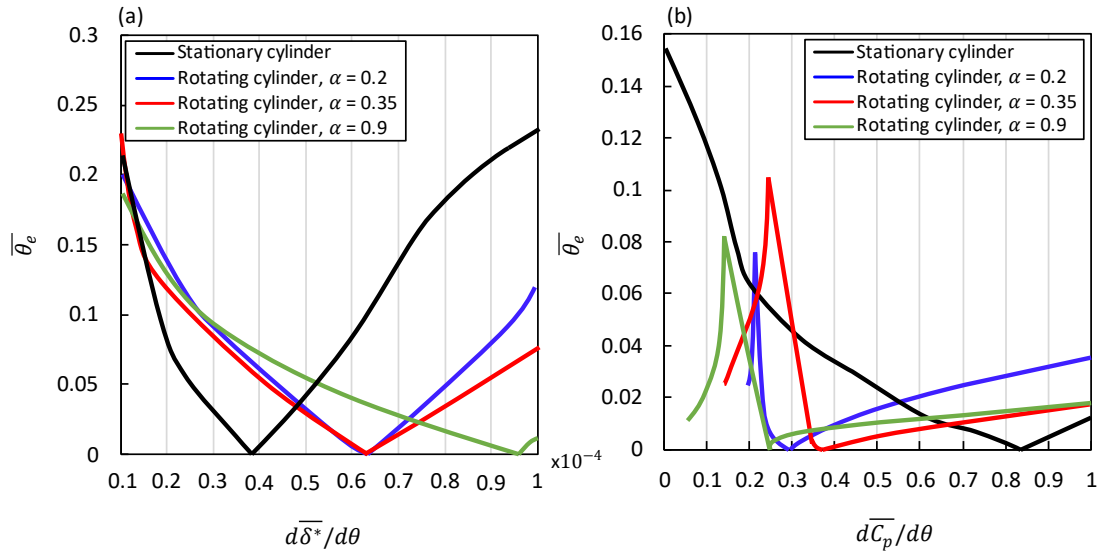


Figure 4.4:  $\overline{\theta}_e$  with respect to gradients of mean displacement thickness in (a), and mean pressure coefficient in (b) at the top side of cylinder. Formulation of  $\overline{\theta}_e$  is given in Equation 4.14.

$$\overline{\theta}_e = \frac{|(\overline{\theta}_s)_{MRS} - \theta|}{(\overline{\theta}_s)_{MRS}}, 0^\circ \leq \theta \leq 180^\circ \quad (4.14)$$

The examinations were performed for each case individually. The locations in which provided minimum  $\overline{\theta}_e$  was considered as critical points to build a new type of separation criterion.

The purpose was to collapse each graph in sufficiently identical criterion value at the  $x$ -axis of the graph at minimum  $\overline{\theta}_e$  position for each case. This provides one definite number which must be reached to prove that flow is separated. In order to shift the curves at a single point, the combinations of the chosen variables were utilized. The ratio of root mean square (RMS) and average of the values that were calculated by the sample criteria expressions were indicated in Table 4.2.

Table 4.2: Separation criteria expressions and RMS/average of outputs at minimum  $\overline{\theta}_e$

Criteria Number	Criteria	$Re(\rho, \mu, \delta^*, U_\infty)$			$Re(\rho, \mu, \delta^*, U_\infty - U_\theta)$		
		RMS/avg	$a$	$b$	RMS/avg	$a$	$b$
1	$\frac{d\overline{C}_p}{d\theta}$	0.76	-	-	-	-	-
2	$\frac{d\overline{C}_p}{d\theta} \left( \frac{d\overline{\delta}^*}{d\theta} \frac{1}{\overline{\delta}^*} \right)^a$	0.32	-0.65	-	0.32	-0.65	-
3	$\frac{d\overline{C}_p}{d\theta} \left( \frac{d\overline{\delta}^*}{d\theta} \frac{1}{\overline{\delta}^*} \right)^a (Re^*)^b$	0.07	2.68	2.51	0.1	-1.09	-0.49
4	$\frac{d\overline{C}_p}{d\theta} (Re^*)^a$	0.26	0.53	-	0.5	0.47	-
5	$\left( \frac{d\overline{\delta}^*}{d\theta} \frac{1}{\overline{\delta}^*} \right)$	1.14	-	-	-	-	-
6	$\left( \frac{d\overline{\delta}^*}{d\theta} \frac{1}{\overline{\delta}^*} \right) \left( \frac{d\overline{C}_p}{d\theta} \right)^a$	0.4	-1.07	-	0.4	-1.07	-
7	$\left( \frac{d\overline{\delta}^*}{d\theta} \frac{1}{\overline{\delta}^*} \right) \left( \frac{d\overline{C}_p}{d\theta} \right)^a (Re^*)^b$	0.03	0.36	0.93	0.09	-0.91	0.44

---

8	$\left(\frac{d\bar{\delta}^*}{d\theta} \frac{1}{\bar{\delta}^*}\right) (Re^*)^a$	0.10	0.72	-	0.48	0.86	-
---	--	------	------	---	------	------	---

---

All the combinations own one repeating parameter that has no exponent. Additional variables are controlled with  $a$  and  $b$  exponents depending on the case. Two different Reynolds numbers are defined, yet the modified Reynolds number is favored due to giving more physical insight for the nature of the current problem. The gradient of displacement thickness is also non-dimensionalized by the appropriate multiplication. In the process of collapse of 4 cases, The RMS value is calculated by using the stationary cylinder case as a reference. The exponents,  $a$  and  $b$ , are extracted where the RMS/average is minimum for the particular criterion. As a result, the third and seventh criteria demonstrate the optimal performance regarding the deviations. In addition, the integration of all variables has a potential to represent the most detailed characterization of separation. These two criteria represent effectively equivalent behavior, however, the third expression is selected as a main criterion. In this expression, the displacement thickness is considered as a factor that must be controlled by an exponent wherefore to control the effect of the shape of the boundary layer thickness. Figure 4.5 shows the shifted curves of all cases by the proposed criterion.

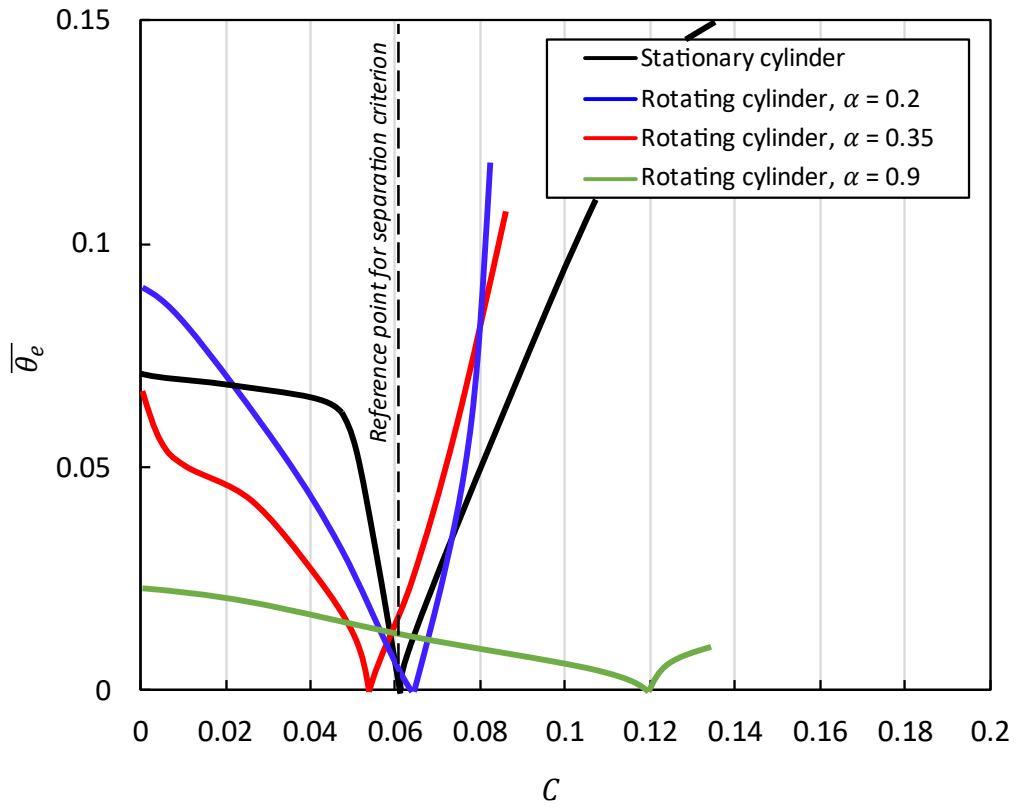


Figure 4.5:  $\bar{\theta}_e$  with respect to criteria outputs

The criteria value ( $C$ ) in stationary case is accepted as a benchmark for the other cases as well. The deviation of the  $C$  value provides the error of the method. The  $C$  value was found as 0.0619. This value is the first milestone while the separation point is searched for. If  $C$  is equal or bigger than 0.0619, separation is formed at that position around the cylinder. In detailed calculations, it was seen that using only this expression is not sufficient due to providing more than one point of separation. In order to eliminate the false separation angles, additional complementary criteria are needed. For the separation, priorly flow must be in the adverse pressure gradient region. In Figure 4.6, graphical demonstration was given.

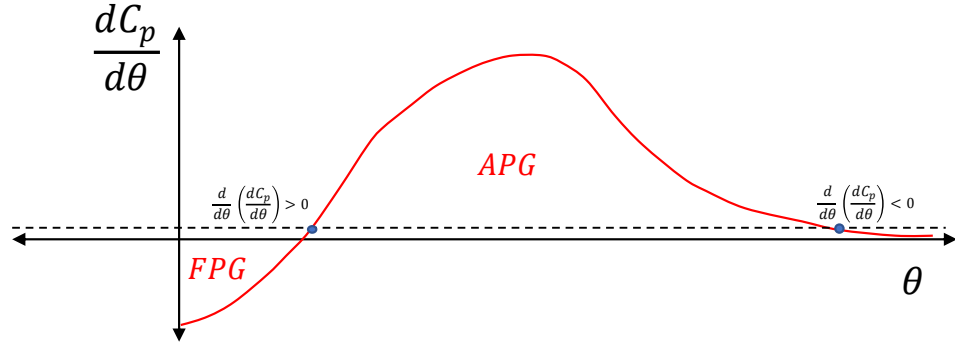


Figure 4.6: Example of pressure gradient distribution

There are two inflection points in the distribution of the pressure gradient. In the first point, the derivative of the pressure gradient is positive which means the flow is entering the adverse pressure gradient region (APG) at that moment. Contrarily, the second point is negative, and flow is detached. Hence, the criterion is extended to the conditions given in the following equations:

$$\frac{d\bar{C}_p}{d\theta} \left( \frac{d\bar{\delta}^*}{d\theta} \frac{1}{\bar{\delta}^*} \right)^a (Re^*)^b \geq C \quad (4.15)$$

$$\frac{d\bar{C}_p}{d\theta} > 0 \quad (4.16)$$

$$\frac{d}{d\theta} \left( \frac{d\bar{C}_p}{d\theta} \right) < 0 \quad (4.17)$$

The method was tested to examine its sensitivity to the variation of  $a$ ,  $b$  exponents and  $C$  value. Primarily the base values of  $a$ ,  $b$  and  $C$  was modified by manual robust optimization. The base values were altered in the band of  $\pm 5\%$  ( $a = -0.9 \pm 5\%$ ,  $b = -0.5 \pm 5\%$ ,  $C = 0.054 \pm 5\%$ ) and Monte Carlo method was implemented. The change of separation angles was observed in a scattered plot. For 4 different cases alteration of the separation angles and their histogram plots were indicated in Figure 4.7.

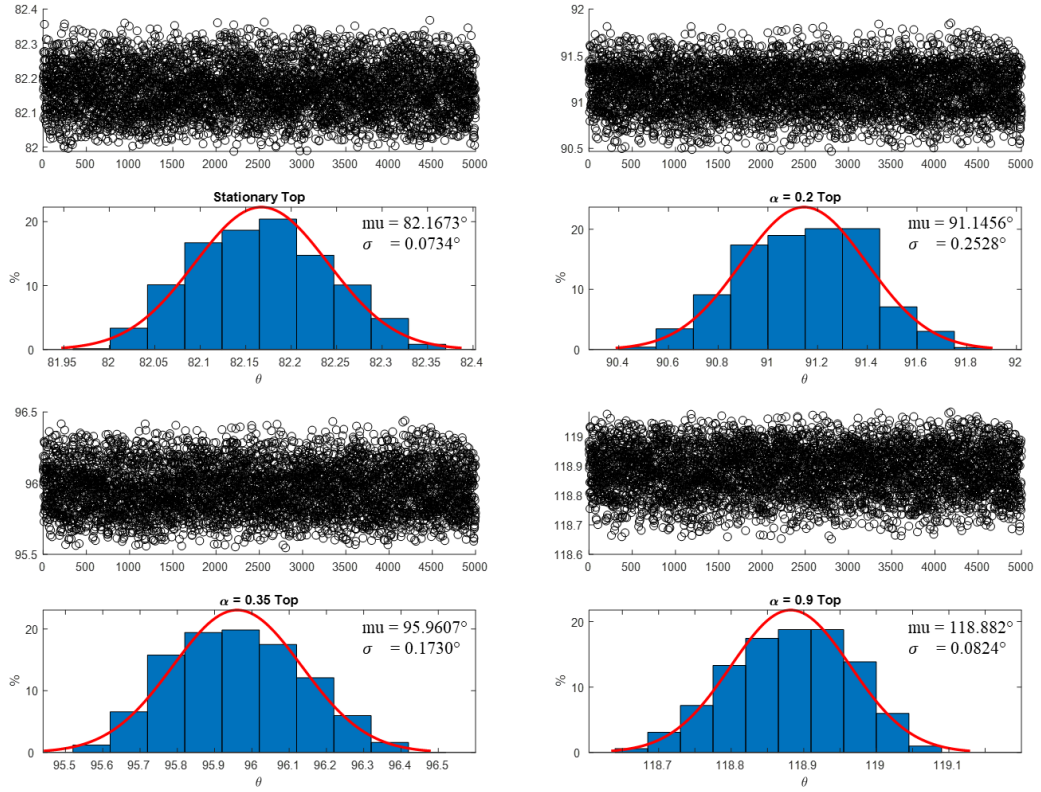


Figure 4.7: Monte Carlo simulations and distribution of separation angles

In the light of the graphs in Figure 4.7, the error calculation was formulated to reach the accuracy of the current separation criterion. Following equations shows the formula of the error.

$$p = \frac{2\sigma_{stationary} + 2\sigma_{\alpha=0.2} + 2\sigma_{\alpha=0.35} + 2\sigma_{\alpha=0.9}}{4} \quad (4.18)$$

$$b = \frac{\Delta\theta_{stationary} + \Delta\theta_{\alpha=0.2} + \Delta\theta_{\alpha=0.35} + \Delta\theta_{\alpha=0.9}}{4} \quad (4.19)$$

$$\Delta\theta = abs\left(\overline{(\theta_s)}_{MRS} - \overline{(\theta_s)}_{MC}\right) \quad (4.20)$$

$$err = \sqrt{p^2 + b^2} \quad (4.21)$$



The Equation 4.18 represents the precision error ( $p$ ) which comes from the bell curve for each case. For the calculation 2 sigma was based on, contributing more than 95% of the population that gives an accurate output. Bias error ( $b$ ) was essentially calculated by using the difference of the separation angle found by MRS criterion and mean values in the bell curves (Equation 4.19 and Equation 4.20). Average of all  $\Delta\theta$  gives the bias error. Root mean square of the precision and bias errors was accessed with the Equation 4.21. Consequently, resulting error for the current method was found  $err \approx \pm 0.4^\circ$ .

After the evaluation of the criterion, separation angles at the top and bottom sides of the cylinder were predicted. Separation and transition onset locations were shown with Table 4.3.

Table 4.3: Separation and transition angles for the test cases. MRS criteria is only used for the receding (top) side. Current separation and transition onset criteria outputs are shown both receding and advancing (bottom) sides with the calculation uncertainties

Cases	$(\overline{\theta_{st}})_{MRS}$ ( $^\circ$ )	$(\overline{\theta_{st}})_C$ ( $^\circ$ )	$(\overline{\theta_{sb}})_C$ ( $^\circ$ )	$\overline{\theta_{tr_t}}$ ( $^\circ$ )	$\overline{\theta_{tr_b}}$ ( $^\circ$ )
$\alpha = 0$	81	$81 \pm 0.4$	$-81 \pm 0.4$	81	-81
$\alpha = 0.2$	92	$91 \pm 0.4$	$-73 \pm 0.4$	89	-73
$\alpha = 0.35$	96	$96 \pm 0.4$	$-130 \pm 0.4$	97	-80
$\alpha = 0.9$	119	$119 \pm 0.4$	$-113 \pm 0.4$	118	-82

In Table 4.3;  $(\overline{\theta_{st}})_{MRS}$  is the top separation angle found by MRS criterion,  $(\overline{\theta_{st}})_C$  is the top separation angle by current criterion,  $(\overline{\theta_{sb}})_C$  is the bottom separation angle by current criterion.  $\overline{\theta_{tr_t}}$  and  $\overline{\theta_{tr_b}}$  represent the top and bottom transition onset angles,

respectively. According to the results, the new separation criterion shows an excellent agreement with MRS criterion at the downstream moving wall. The advantage of this criterion is of being useful in the upstream moving wall as well. At the bottom side of the cylinder (upstream moving wall), Reynolds number expression was altered by the guide of Equation 4.13, providing physical robustness. As estimated in rotating  $\alpha = 0.2$  and  $\alpha = 0.9$  cases, top separation actualizes later than the bottom separation meaning the conventional Magnus effect. Conversely, the separation occurs far beyond in the bottom at  $\alpha = 0.35$  which proves that the obligations of inverse Magnus effect are achieved, and the criterion works well. At that case, the type of boundary layer separation at the top is laminar, and at the bottom is vice versa.

## 4.2 Inverse Magnus effect by circulation control using partially rotating boundaries

The validation of the numerical model and criteria for separation and transition was succeeded, thereof the pre-targeted investigation was immediately initiated. In order to investigate conventional and inverse Magnus effect, a novel geometry is proposed. In the new geometry, instead of fully rotation, the cylinder has 4 partially rotating surfaces which can be actuated on clockwise direction. Referred cylinder geometry is given in Figure 4.8.

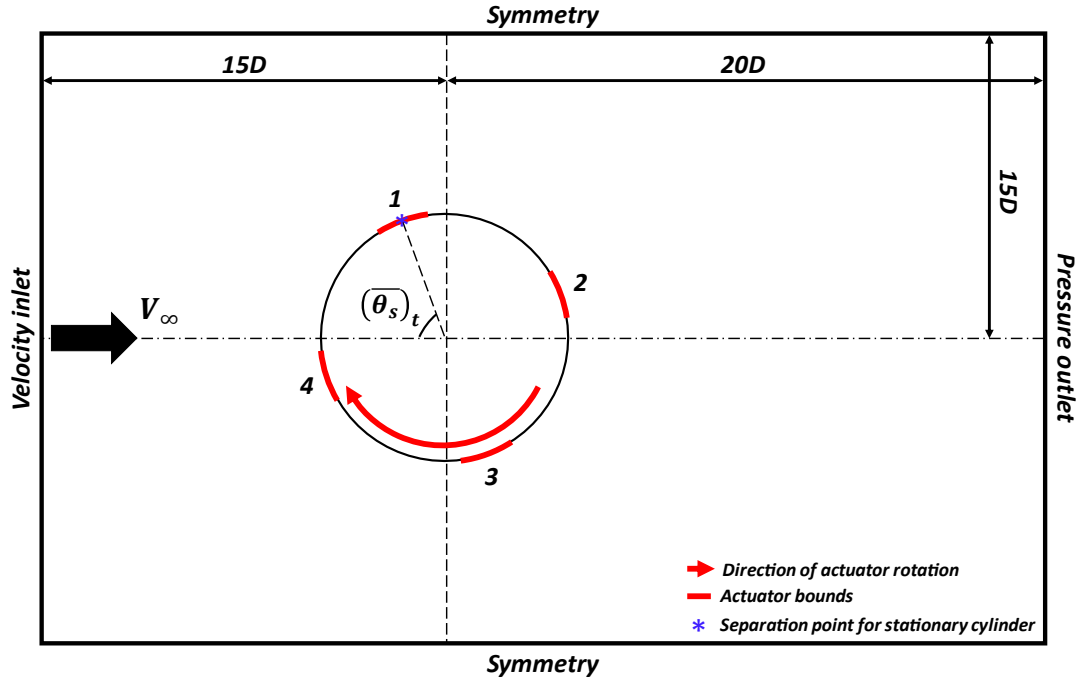


Figure 4.8: Circular cylinder inside the flow domain with the boundary conditions.

Stationary cylinder with enumerated 4 actuators rotating clockwise direction. The first actuator is located where the flow separates on the top of the stationary cylinder

$$\left( (\overline{\theta}_s)_t = 81^\circ \right).$$

In the inverse Magnus effect, the main purpose is to reach early laminar separation at the receding side which is needed local Reynolds number decrease. This is the reason of the moving surfaces (actuators) are located regarding the separation angle at the top side that is found for stationary cylinder. The center point of the first actuator surface is directly matched to the  $81^\circ$ , measured from the upstream stagnation point. Specifically, reaching the inverse Magnus effect is the top priority in this study, however in appropriate conditions, the conventional Magnus forces can also be obtained with this unique geometry. After the positioning of the first actuator, other actuators are placed with a  $90^\circ$  order with respect to each other. In the context of this study, all the active surfaces are conceived identical and cover a partial surface that corresponds an angular segment of  $14^\circ$ , approximately. This area is calculated based on the experimental concept given in appendix. The actuators help to control the circulation both in the wall surface and the flow. Solution method, mesh and time step

features are kept identical with the stationary and fully rotating cylinder cases. Following sections contain the simulation results and the optimization.

#### 4.2.1 Comparison of fully and partially rotating cylinders

Partially rotating cylinder case was numerically investigated for different spin ratios. The Reynolds number was fixed at 128000, using the same temporal and spatial conditions in the numerical model. Time-averaged lift and drag coefficients were extracted and compared to the past and current studies which includes fully rotating cylinder results. The tangential velocity at the cylinder wall is used to calculate the spin ratio ( $\alpha$ ) with the stream velocity for fully rotating body. In partially rotating cylinder, the foundation of the spin ratio is identical, however, the total wall circulation is not equal to the fully rotating case. Therefore, the equivalent comparison is only executed by matching the wall circulation ( $\overline{\Gamma_w}$ ) which are not the same at identical spin ratios. The calculation of the  $\overline{\Gamma_w}$  is represented in Equation 4.22.

$$\overline{\Gamma_w} = \frac{\alpha_1 A_1 + \alpha_2 A_2 + \alpha_3 A_3 + \alpha_4 A_4}{A_1 + A_2 + A_3 + A_4} \quad (4.22)$$

For the fully rotating case  $\overline{\Gamma_w}$  is exactly even to the spin ratio. On the contrary, due to the moving surfaces are restricted in partially rotating body, obtaining the circulation is essential for the robust interpretation. In the equation,  $A$  is the area and  $\alpha$  is the spin ratio for each actuator.  $\overline{\Gamma_w}$  is found as a function of  $\alpha$ . Figure 4.9. contains the aerodynamic force coefficients from the Swanson's fully rotating experimental data [9], recent numerical data for fully rotating cylinder and the partially rotating simulations.

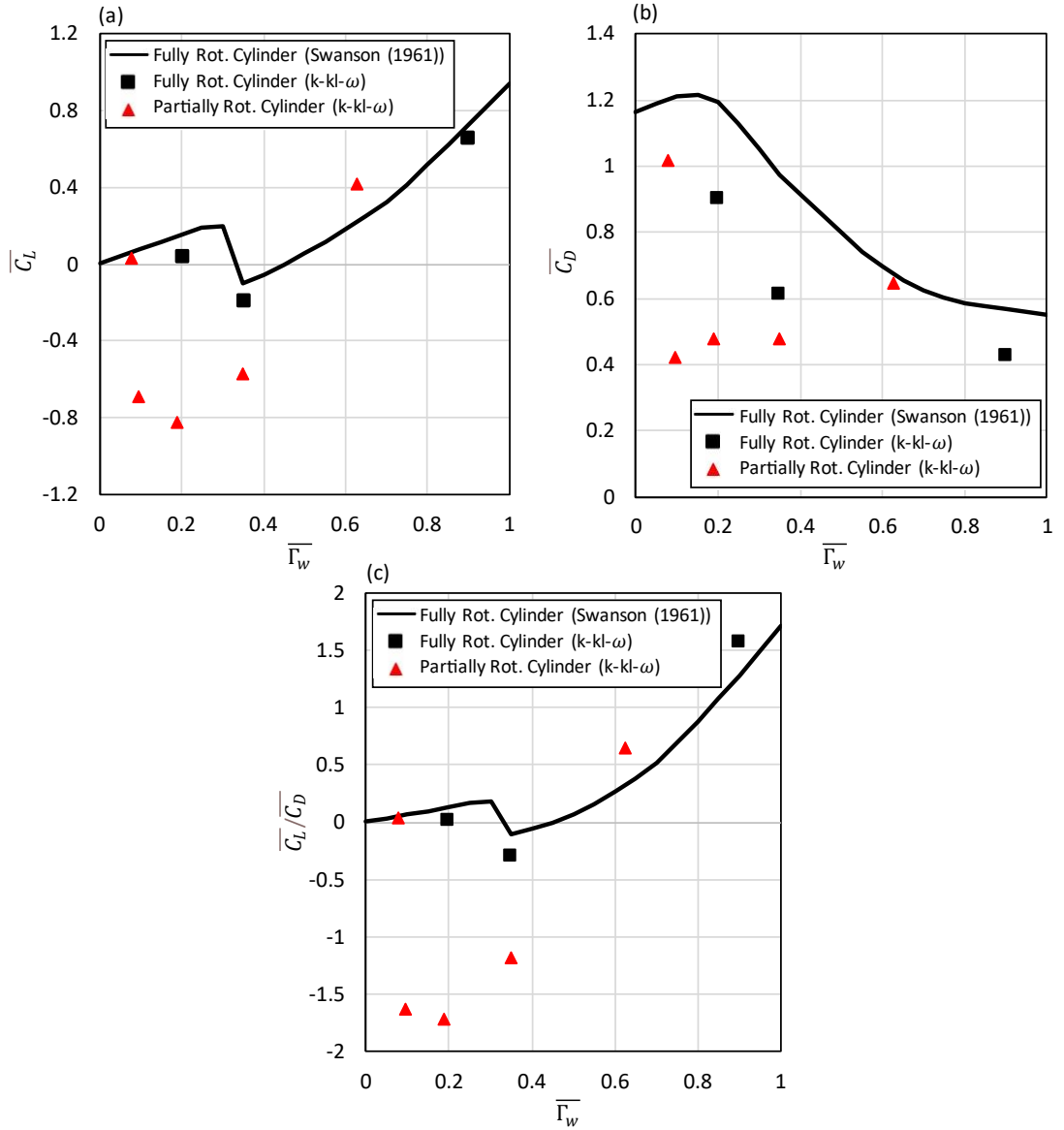


Figure 4.9: Fully and partially rotating cylinder cases are compared in time-averaged aerodynamic force coefficients. (a) Lift coefficient, (b) drag coefficient, (c) lift-to-drag coefficient. The x-axis corresponds weighted-average wall circulation (Equation 4.22)

The actuator enabled case depicts far different tendency compared to the fully rotating cases. Sudden fall in lift is observed at around  $\overline{\Gamma_w} = 0.35$  in fully rotating cylinder. On the other hand, same decrease occurs at  $\overline{\Gamma_w}$  value less than 0.1 in partially rotating cylinder. This behavior points out the effectiveness of local circulation control on inverse Magnus effect. Negative lift forces are achieved by

lower tangential velocities which is one of the main advantages of current geometry. Besides that, if the minimum lift values are contrasted in two cases, it can be observed that partially rotating cylinder promises the highest lift in negative direction. In that case, the lift coefficient reaches the minimum towards  $\overline{\Gamma}_w = 0.2$ , then start to increase in positive direction. According to the curve of the simulation results, flow changes its manner to the conventional Magnus at somewhere between  $\overline{\Gamma}_w = 0.5 - 0.6$ . The key point is specified to investigate the aerodynamic coefficients as a ratio of lift-to-drag coefficients. The reason is that to increase lift in negative sign, decrease the drag simultaneously, meaning higher lift-to-drag coefficient in the negative course, aiming to search the boundaries of the geometry proposed.

At  $\overline{\Gamma}_w = 0.35$ , all cases are resulted with the inverse Magnus effect. Therefore, at this circulation value, comparisons and interpretations can be performed comprehensively. In Table 4.4, the separation angles calculated by current criterion and aerodynamic force coefficients were submitted.

Table 4.4: Simulation outputs of compared cases (fully and partially rotating cylinders) at  $\overline{\Gamma}_w = 0.35$ .

$\overline{\Gamma}_w = 0.35$	$\overline{C}_L$	$\overline{C}_D$	$\overline{C}_L/\overline{C}_D$	$(\overline{\theta}_s)_t$ (°)	$(\overline{\theta}_s)_b$ (°)
Fully rotating cylinder	-0.19	0.6	-0.3	96±0.4	-130±0.4
Partially rotating cylinder	-0.6	0.5	-1.2	98±0.4	-124±0.4

The lift-to-drag coefficient at a given  $\overline{\Gamma}_w$  is far greater at partially rotating case. The first application of the separation criteria is resulted unsuccessfully for the partially rotating cylinder case. The calculated separation angle support the type of Magnus

effect, however, when the separation location is checked by the velocity vectors, it is observed that, at that location the flow is already separated and the reverse flow region occurs before the separation point that is found by current criterion. Luckily, all flow separation points run into the stationary areas on a partially actuated cylinder. Therefore, for the detecting the separation, the conventional method was used ( $\partial u/\partial n = 0$ ).

#### 4.2.2 Sensitivity analysis and gradient descent optimization of actuator configurations

The configuration of the actuators is an issue that must be investigated in current geometry. At selected  $\overline{\Gamma_w}$  value, the rotational velocities of the actuators are optimized to obtain the maximum lift-to-drag in reverse order. Essentially, each actuator has the same rotational velocity at the beginning without holding any information about the effectiveness of each actuator individually. Therefore, the weights of the actuators are calculated as a matter of priority. The sensitivity calculation is executed by perturbing each velocity in one time. Then found values are projected to the selected  $\overline{\Gamma_w}$ . The perturbation process is carried out 15% forward increment in velocity for all rotating surfaces. The new velocity configurations are implemented on additional simulations. Each result offers an insight to the influence of each actuator on  $\overline{C_L}/\overline{C_D}$ . The case which all the moving surfaces has the same velocity is called the nominal case. The gradients of  $\overline{C_L}/\overline{C_D}$  with respect to change of velocity is found by the difference among the nominal and perturbed cases. In order to find the optimum configuration inside the restriction of  $\overline{\Gamma_w}$  at 4-dimensional space, the projected gradient descent method [49] is utilized. This method includes an unknown vector  $s(k)$  which minimizes the expression in Equation 4.23:

$$\|x(k) - \nabla F(x(k)) - s(k)\| \quad (4.23)$$

subject to the constraint that  $\mathbf{I} \cdot s(k) - \mathbf{I} \cdot x(1) = 0$ .  $\nabla F(x(k))$  is the gradient of  $\overline{C_L}/\overline{C_D}$  by the change of the velocities and  $x(k)$  is the initial or former step for the optimization. Next step calculation is given by the Equation 4.23.

$$x(k + 1) = x(k) + \gamma(s(k) - x(k)) \quad (4.23)$$

Here  $s(k) - x(k)$  gives the direction vector and  $\gamma$  is the step size through that direction. Upper and lower bounds of the rotational velocity are decided according to the formula,

$$N_{max} = \pm(N_{nominal} + 2N_{nominal}) \quad (4.24)$$

which the maximum step size is chosen by.  $N$  is the velocity in rpms. This method ensures that the constraint of  $\overline{\Gamma_w}$  is satisfied at all steps. After the implementation of the projected gradient descent method,  $\gamma$  is changed between zero and  $\gamma_{max}$  to evaluate the alteration of  $\overline{C_L}/\overline{C_D}$  at presented path. The  $\gamma$  values are chosen reasonably regarding to the developed trend during the process to decrease the total computational time. The global minima (maxima in negative direction) are accessed after two steps of optimization methodology. In Figure 4.10, the whole process of the projected gradient descent (PGD) optimization is indicated.



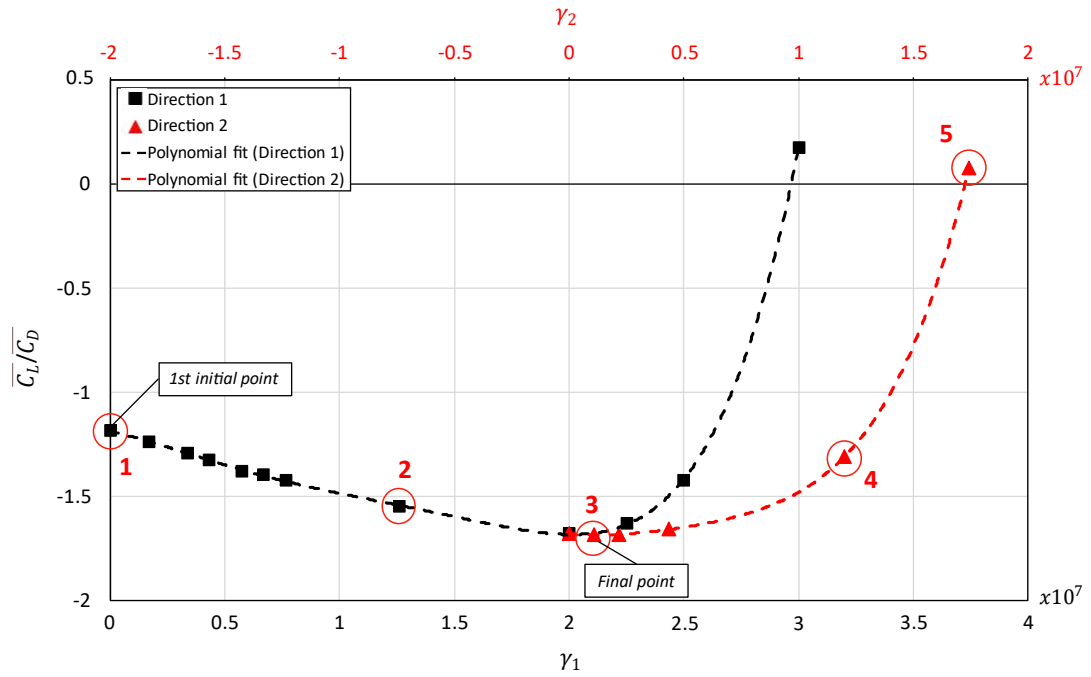


Figure 4.10:  $\overline{C_L}/\overline{C_D}$  with respect to step size as a result of PGD method

The Figure 4.10 includes two stages of PGD optimization. The first direction provides around 41.6% of significant increase in lift-to-drag coefficient compared to the nominal case (initial point). This improvement is handled as a guideline for the second direction to march on. The recommended second direction by PGD is considered and extra development is acquired (41.95% w.r.t initial location) as  $\overline{C_L}/\overline{C_D} = -1.686$ . Between the final point and the second initial point, there is around 0.24% rise, justifying the convergence of the optimization transactions. Next step is to compare the alteration of physics of the different cases during the optimization. In Figure 4.10, five different cases are marked with the significant numbers. These cases are compared in the Figure 4.11, providing; separated, attached and turbulent regions on the wall surface, mean stream functions,  $u = 0$  lines and  $u$ -velocity contours.

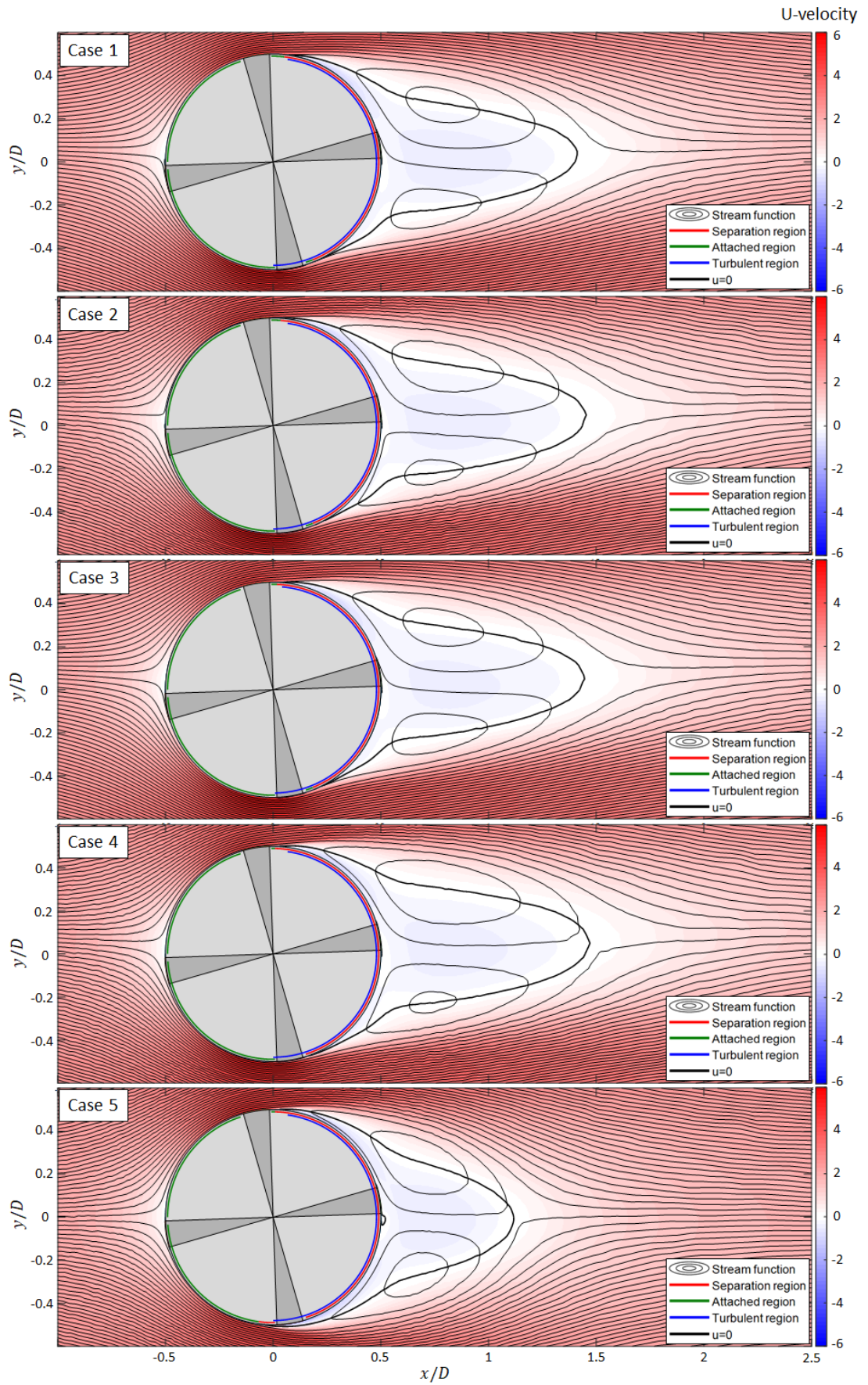


Figure 4.11: Mean streamlines with the locations of transition onset and separation

The time-averaged streamlines indicate the level of the inverse Magnus forces. For the partially rotating cases, the dark segments onto the cylinder represents the positions of the actuators. The increment of lift-to-drag coefficient triggers the rise of the flow angle with respect to streamwise direction. Nevertheless, the position of the front stagnation point is shifted towards the receding side. This appearance is clearly observed from case 1 to case 3. The flow angle slightly increases when the lift increases on partially rotating cylinder cases. Apparently, the bottom half of the wake region is downsized as a result of upwards flow movement and increased flow angle. The front stagnation point has also an obvious dislocation throughout where the flow direction is opposite to the wall movement. All these flow characteristics induce the high lift in inverse Magnus effect. The separation and transition onset angles are also the indicators of the type of Magnus effect. In Figure 4.11, the locations are visually observed, and except case 5, it is proved that the inverse Magnus effect takes place. In purpose of having more quantitative sense, the location of front stagnation point and the fraction of the separated regions were calculated at each case. Front stagnation point was found on the location where the surface pressure is maximum and the streamwise velocity is zero. The formulation of fraction of separated flow region is given with Equation 4.25.

$$f_s = \frac{A_s}{A_a + A_s} \quad (4.25)$$

There;  $f_s$ ,  $A_s$  and  $A_a$  corresponds the fraction of separation, the area of the separated flow region and the area of the attached flow region on cylinder surface. The fraction of separation was quantified at both the receding and advancing sides. In this way, it is aimed to explain the connection of separation points at each side by the relative difference and the amount of variation of separated regions. Due to the lack of effectiveness of current separation criterion, the separation locations were detected by using traditional method that uses zero-shear stress location. The physics of partially actuated case makes that determination possible; according to the velocity vectors, the separation has formed on the stationary regions on the cylinder in all cases. In Table

4.5, angle of the front stagnation points ( $\overline{\theta_{sp}}$ ), the lift-to-drag coefficients, the fractions of separation and the rotational velocities of all cases are shown.

Table 4.5: Comparison of selected 5 cases with different variables

Case	$f_s$			$\overline{C_L}/\overline{C_D}$	$\overline{\theta_{sp}}$	$N_{A1}$ (rpm)	$N_{A2}$ (rpm)	$N_{A3}$ (rpm)	$N_{A4}$ (rpm)
	Top	Bottom	Overall						
1	0.5153	0.4277	0.472	-1.187	3.7	3046.8	3046.8	3046.8	3046.8
2	0.5276	0.4277	0.4783	-1.552	4.8	2287.6	2509.4	2047	5343.3
3	0.5399	0.4277	0.4845	-1.686	5.3	1780.6	2265.1	1417.3	6724.3
4	0.546	0.4528	0.5	-1.311	4.8	1146.9	2967.1	964.65	7108.6
5	0.546	0.5094	0.528	0.0758	0.3	832.2	3315.7	739.8	7299.5

Angle of the front stagnation point is calculated in the positive direction towards  $90^\circ$ , assuming the upstream of the cylinder is  $0^\circ$ . As seen in Table 4.5, from case 1 to 3, the stagnation location shifts to the receding side with the increase of  $\overline{C_L}/\overline{C_D}$  in negative direction. That causes flow at the bottom side of the cylinder travels more distance after the stagnation point, providing the rise of the local turbulence level at the advancing side. That means more momentum transfer by turbulence, pushing the flow upwards and increasing the strength of negative lift force. That shift points out the effectiveness of actuator 4. Until case 3, the increment of actuator 4 influences the flow physics positively. However, although the velocity of actuator 4 raises, the negative  $\overline{C_L}/\overline{C_D}$  drops at case 3 to 5. At case 4 stagnation point tends to shift advancing side, eventually at case 5 conventional Magnus effect takes place with a  $\overline{\theta_{sp}}$  almost located at the horizontal center of the cylinder. This indicates that the actuator 4 may have a certain rise limit or the actuators 2 and 3 may have a certain decrease limit. The variation of  $\overline{C_L}/\overline{C_D}$  can also be explained by the fraction of separation. During the

optimization, until the case 3, the bottom fraction remains constant, on the contrary the top fraction of separation has an increment. This condition refers that the separation at the top arises earlier case by case which is expected condition for more intense reverse Magnus force. The rise of the fraction continues at the receding side in case 4, nonetheless bottom fraction is enhanced much more than top side, clarifying the decrease of negative lift force. Ultimately,  $f_s$  at the bottom rises massively with the transformation to the conventional Magnus effect.

# Chapter 5

## Conclusion

The inverse Magnus effect has a unique nature, only valid in specific conditions. These conditions can be constituted by appropriate Reynolds number and spin ratio. This study covers the whole process of inducing inverse Magnus effect around circular cylinder. The purpose of the study is to create this effect without full body rotation. Four identical rotating segments are located onto the cylinder surface, providing partial circulation control to stimulate inverse Magnus force which is an imitation of fully rotating cylinder locally. By changing the configuration of actuated surfaces, the manageable nature of the inverse lift is represented. The post-process is the most formidable part of the interpretation in inverse Magnus effect. Even if the right lift and drag values are obtained, the validation of this phenomenon is executed with observing mostly the flow physics. In this context, the relative location of the flow separation of each side, the kind of separation, transition to turbulence onset location, the circumferential pressure distribution, the strain rate distribution in the flow domain and streamlines are the crucial elements to find a clue from inverse Magnus effect. These parameters are mostly useful to predict the formation mechanism of this physical state. The most important part of the post-process is achieved by proposing novel criteria for marking the separation and transition onset location at both sides of the cylinder. Successful predictions of these critical locations are reached with a small amount of uncertainty. The indications prove the literature; the receding side (top side of the cylinder in current case) has always laminar boundary layer separation, since the advancing (bottom side of the cylinder in current case) characterized by the turbulent separation, causing later separation at the advancing side. The delayed separation at the bottom side changes the flow direction upwards, developing the force towards the bottom which is inverse Magnus effect in this setup. These flow directions are indicated significantly in the image of the streamlines. All the methodology is

repeated for various fully and partially rotating cylinder cases. In order compare the partial actuated cylinder with the fully rotating cylinder, the total surface circulation ( $\overline{\Gamma_w}$ ) is kept constant. At particular  $\overline{\Gamma_w}$ , it is perceived that the partially rotating cylinder provides higher negative lift than fully. Afterwards, by altering the configuration of actuators with the projected gradient descent optimization, lift-to-drag coefficient is enhanced more in negative direction which ensures 466% rise compared to the fully rotating cylinder.

The Magnus forces are utilized recently in mostly conceptual designs to govern the aerodynamic forces acting on aircraft. The more sophisticated understanding based on theoretical studies take an important role for the advancements in this field of study. The information and novelty of this work is believed to have crucial contribution to this topic and beyond. It is predicted that the current study will be a guide with its important outputs in the use of the Magnus effect on controlling lift and drag forces acting on various structure, such as, airfoils, rotors of Flettner ships, crafts and possibly even some critical buildings exposed to the strong flow curenents. In the near future, it is planned to build an experimental setup for supporting the numerical study and extending the limits of the inverse Magnus effect in a practical approach.

# References

- [1] Schlichting H, Gersten K. Boundary-layer theory, 9th ed. Springer; 2016.
- [2] Magnus G. Ueber die Abweichung der Geschosse, und: Ueber eine auffallende Erscheinung bei rotirenden Körpern. *Annalen der physik* 1853; 164(1): 1-29.
- [3] Lafay A. Sur l’Inversion du phenomene de Magnus. *Comptes Rendus Hebdomadaires des Séances de l’Académie des Sciences* 1910; 151: 867-868.
- [4] Kray T, Franke J, Frank W. Magnus effect on a rotating soccer ball at high Reynolds numbers. *Journal of Wind Engineering and Industrial Aerodynamics* 2014; 124: 46-53.
- [5] Miyazaki T, Sakai W, Komatsu T, Takahashi N, Himeno R. Lift crisis of a spinning table tennis ball. *European Journal of Physics* 2016; 38(2): 024001.
- [6] Lyu B, Kensrud J, Smith L. The reverse Magnus effect in golf balls. *Sports Engineering* 2020; 23(1): 3.
- [7] Lafay A. Contribution experimentale a l’aerodynamique du cylindre. *Reveus Mechanique* 1912; 30: 417-442.
- [8] Krahn E. Negative magnus force. *Journal of the Aeronautical Sciences* 1956; 23(4): 377-378.
- [9] Swanson WM. The Magnus effect: A summary of investigations to date. *Journal of Basic Engineering* 1961; 83(3): 461-470.
- [10] Fletcher CA. Negative Magnus forces in the critical Reynolds number regime. *Journal of Aircraft* 1972; 9(12): 826-834.



- [11] Maruyama Y. Study on the physical mechanism of the Magnus effect. Transactions of the Japan Society for Aeronautical and Space Sciences 2011; 54(185+186); 173-181.
- [12] Muto M, Tsubokura M, Oshima N. Negative Magnus lift on a rotating sphere at around the critical Reynolds number. Physics of Fluids 2012; 24(1): 014102.
- [13] Kray T, Franke J, Frank W. Magnus effect on a rotating sphere at high Reynolds numbers. Journal of wind engineering and industrial aerodynamics 2012; 110: 1-9.
- [14] Kusyumov AN, Romanova EV, Batrakov AS, Nurmukhametov RR, Barakos GN. Simulation of the flow around a rotating circular cylinder taking into account laminar-turbulent transition. Russian Aeronautics (Iz VUZ) 2013; 56(2): 145-153.
- [15] Zheng Z, Lei J, Wu X. Numerical simulation of the negative Magnus effect of a two-dimensional spinning circular cylinder. Flow, Turbulence and Combustion 2017; 98(1): 109-130.
- [16] Kim J, Choi H, Park H, Yoo JY. Inverse Magnus effect on a rotating sphere: when and why. Journal of Fluid Mechanics 2014; 754.
- [17] Cheng W, Pullin DI, Samtaney R. Large-eddy simulation of flow over a rotating cylinder: the lift crisis at  $Re_D = 6 \times 10^4$ . Journal of Fluid Mechanics 2018; 855: 371-407.
- [18] Thom A. Effect of discs on the air forces on a rotating cylinder. HM Stationery Office 1934.
- [19] Aljure DE, Rodríguez I, Lehmkuhl O, Pérez-Segarra CD, Oliva A. Influence of rotation on the flow over a cylinder at  $Re = 5000$ . International Journal of Heat and Fluid Flow 2015; 55: 76-90.
- [20] Carstensen S, Mandviwalla X, Vita L, Paulsen US. Lift of a rotating circular cylinder in unsteady flows. In: The Twenty-second International Offshore and

Polar Engineering Conference. International Society of Offshore and Polar Engineers; 2012 Jun 17-21; Greece.

- [21] Nguyen S, Corey M, Chan W, Greenhalgh ES, Graham JMR. Experimental determination of the aerodynamic coefficients of spinning bodies. *The Aeronautical Journal* 2019; 123(1263): 678-705.
- [22] Modi V. On the moving surface boundary-layer control. In: *Fluids 2000 Conference and Exhibit*; Jun 19-22; USA.
- [23] Courant R, Friedrichs K, Lewy H. Über die partiellen Differenzgleichungen der mathematischen Physik. *Mathematische annalen* 1928; 100(1): 32-74.
- [24] Rosetti GF, Vaz G, Fajarra AL. URANS calculations for smooth circular cylinder flow in a wide range of Reynolds numbers: solution verification and validation. *Journal of Fluids Engineering* 2012; 134(12).
- [25] Williamson CH. Vortex dynamics in the cylinder wake. *Annual review of fluid mechanics* 1996; 28(1): 477-539.
- [26] Menter FR, Langtry RB, Likki SR, Suzen YB, Huang PG, Völker S. A Correlation-Based Transition Model Using Local Variables—Part I: Model Formulation. *ASME. J. Turbomach.* 2006; 128(3): 413–422.
- [27] Walters DK, Leylek JH. A new model for boundary layer transition using a single-point RANS approach. *J. Turbomach.* 2004; 126(1): 193-202.
- [28] Patankar S. *Numerical heat transfer and fluid flow*. Taylor & Francis; 2018.
- [29] Versteeg HK, Malalasekera W. *An introduction to computational fluid dynamics: the finite volume method*, 2nd ed. Pearson education; 2007.
- [30] ESDU, 1985, “Circular Cylindrical Structures: Dynamic Response to Vortex Shedding, Part 1: Calculation Procedures and Derivation,” Tech. Rep. Item No. 85038, Engineering Sciences Data Unit (ESDU), ESDU International, London.
- [31] Franzini, GR, Meneghini, JR, Gonçalves RT, Fajarra AL. Experimental forces measurements on the flow around a fixed and yawed cylinder in the presence of

- free-surface. In: The Twenty-second International Offshore and Polar Engineering Conference. International Society of Offshore and Polar Engineers; 2012 Jun 17-21; Greece.
- [32] Wu MH, Wen CY, Yen RH, Weng MC, Wang AB. Experimental and numerical study of the separation angle for flow around a circular cylinder at low Reynolds number. *Journal of Fluid Mechanics* 2004; 515: 233-260.
- [33] Achenbach E. Distribution of local pressure and skin friction around a circular cylinder in cross-flow up to  $Re = 5 \times 10^6$ . *Journal of Fluid Mechanics* 1968; 34(4): 625-639.
- [34] Tennekes H, Lumley, JL. *A first course in turbulence*. MIT press; 2018.
- [35] Fluent ANSYS. *Ansys fluent theory guide*. ANSYS Inc. 2011; 15317: 724-746.
- [36] Kline SJ, Reynolds WC, Schraub FA, Runstadler PW. The structure of turbulent boundary layers. *Journal of Fluid Mechanics* 1967; 30(4): 741-773.
- [37] Belotserkovsky SM, Kotovskii VN, Nisht MI, Fedorov RM. *Two-dimensional separated flows*. CRC Press; 1992.
- [38] Moore FK. On the separation of the unsteady laminar boundary layer. *Grenzschichtforschung/Boundary Layer Research*. Springer, Berlin, Heidelberg, 1958; 296-311.
- [39] Rott N. Unsteady viscous flow in the vicinity of a stagnation point. *Quarterly of Applied Mathematics* 1956; 13(4): 444-451.
- [40] Sears WR. Some recent developments in airfoil theory. *Journal of the Aeronautical Sciences* 1956; 23(5): 490-499.
- [41] Koromilas CA, Telionis DP. Unsteady laminar separation: an experimental study. *Journal of Fluid Mechanics* 1980; 97(2): 347-384.
- [42] Sears WR, Telionis DP. Boundary-layer separation in unsteady flow. *SIAM Journal on Applied Mathematics* 1975; 28(1): 215-235.

- [43] Ludwig G. An experimental investigation of laminar separation from a moving wall. In: Aerospace Sciences Meeting; 1964 Jan 20-22; USA.
- [44] Inoue O. MRS criterion for flow separation over moving walls. Aiaa Journal 1981; 19(9): 1108-1111.
- [45] O'Brien V. Two types of instream stagnation. AIAA journal 1984; 22(3): 337-339.
- [46] Peller H. Thermofluiddynamic experiments with a heated and rotating circular cylinder in crossflow. Experiments in fluids 1986; 4(4): 223-231.
- [47] Degani AT, Walker JDA, Smith FT. Unsteady separation past moving surfaces. J Fluid Mech 1998; 375: 1-38.
- [48] Yapalparvi R, Van Dommelen LL. Numerical solution of unsteady boundary-layer separation in supersonic flow: upstream moving wall. Journal of fluid mechanics 2012; 706: 413.
- [49] Drummond LG, Iusem AN. A projected gradient method for vector optimization problems. Computational Optimization and applications 2004; 28(1): 5-29.

# Appendices

# Appendix A

## Experimental setup design for future work

For the upcoming work, the design of the experimental setup is completed for a novel the geometry. The image of the concept of the test rig is given with Figure A.1.

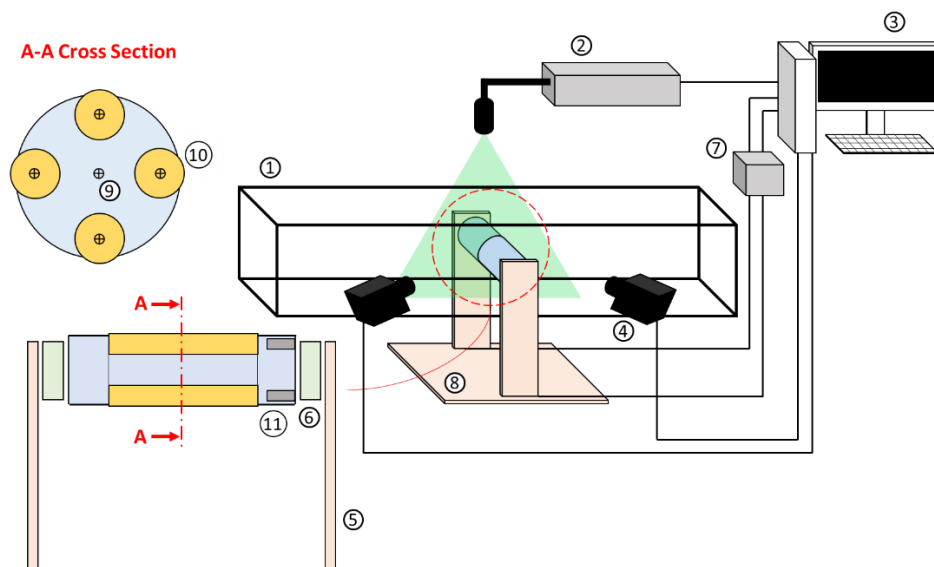


Figure A.1: Elements of the experimental setup, (1) Water tunnel test section, (2) Laser, (3) Computer, (4) High speed camera, (5) Force balance rod, (6) Load cell, (7) Amplifier, (8) Balancing table, (9) Stator, (10) Rotor (actuator), (11) DC-Motor

Modi [22] proposes a unique geometry consisting of rotating small cylinders on a cylindrical stator inspiring the current study. On the stator, 4 identical actuators (rotors)

are placed in an order of  $90^\circ$  between each other. For the parametric study, five degrees of freedom is given to the actuators. The rotational velocity of the rotors can be adjusted in the limits of the DC-motors, additionally their angular positions can also be altered. DC-motors are utilized to rotate each actuator individually. Primarily, the force (lift and drag forces) measurements are performed with the two 3-axis load cells. During the experiments, signals obtained from load cells are amplified for monitoring simultaneously. In addition, PIV measurements system is mounted on the test section. This system involves one class 4 laser, two high speed cameras, computer, and the post-processing software. Obtained PIV images and force data are planned to be combined and be interpreted together for better understanding of the physics. The most crucial topic is to observe the inverse Magnus effect and understanding its relationship with the flow characteristics.

Whole test rig works inside a water tunnel. Therefore, sealing solutions are provided all around the setup. Motors and encoders are kept apart from water as far as possible by these sealing element and construction of the test rig. Waterproof bearings were placed rotor ends to prevent leakage inside the whole system. In, Figure A.2b and Fig. A.2c, the visualization of the experimental setup and, in Fig. A.2a, cross section of the whole system is represented. Test mechanism has the identical components on both ends. From left to right (see Fig. A.2a), force balance rod, load cell, flange among the load cell to the motor housing, motor housing and the motors, coupling housing and the couplings, bearings and shaft sealings may be seen, respectively. The connection between the motors and the rotors are procured by Oldham type couplings. Shaft seals are placed inside where the sealed bearings are located prevents the potential danger by water. In order to restrain the water leakage outside of the water tunnel, fabric penetration seal is used between the test rig and the side walls of the tunnel. This material gives six degrees of freedom for appropriate force measurements. Whole test section is hanged only to the force balance rods. Rotors are located inside the stator. The gap between rotor and stator are adjusted as  $200\mu\text{m}$ , where the motor power and the torque are suitable to work on that condition. Eventually, each part is designed in regards of manufacturability and feasibility. Most of the components are already collected and the assembly process will be initiated in the immediate future.

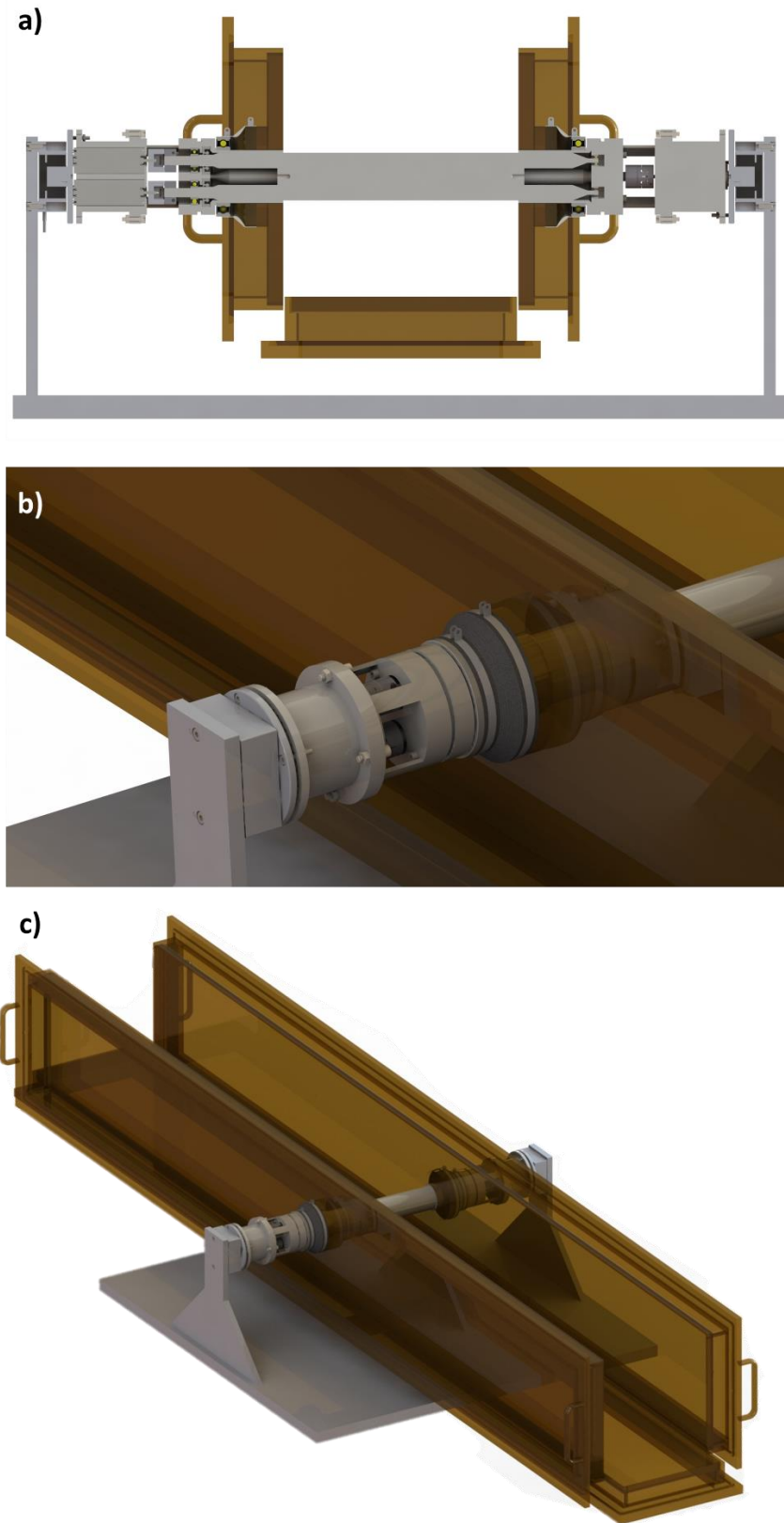


Figure A.2: (a) Cross section of the system, (b) Detailed look of sealing and driver section, (c) Experimental test section



# Appendix B

## Validation of optimization methods

In order to find the best gradient based optimization method fit the current study, performances of two different methods, such as, Frank-Wolfe (FW) method as well as projected gradient descent method (PGD) were investigated on a sample three variable function. A well-behaved convex function is considered which produces a spherical distribution centered at (0, 1, 0) of the form:

$$F(x) = x_1^2 + (x_2 - 1)^2 + x_3^2, \quad x = (x_1, x_2, x_3)$$

Note that we are assuming a convex function, so all gradient descent methods should be on their best behavior.  $G$  is defined as a constraint that is similar with the total circulation in the recent problem:

$$G = x_1 + x_2 + x_3$$

The purpose is to find best first optimization step starting from arbitrary initial point, regarding the optimal direction by minimizing the function that is given earlier. The difference of method results with respect to the optimal direction indicates which algorithm is appropriate to use.

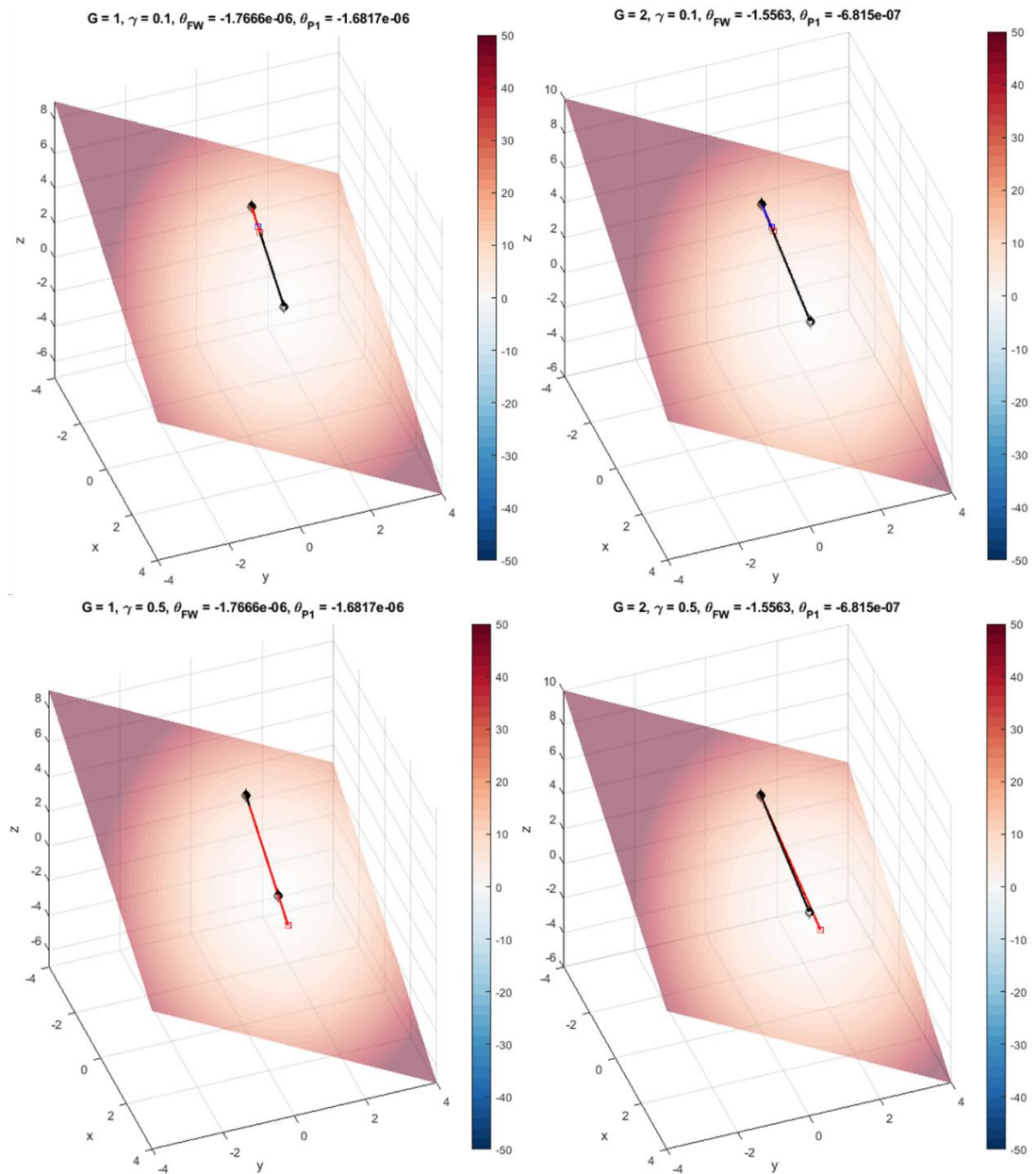


Figure B.1: Comparison of paths: blue line is Projected gradient descent method; red line is Frank-Wolfe method; black line is optimal path.  $G$  and  $\gamma$  are adjusted.

Consider the angle  $\theta$  between the direction recommended by each algorithm and the optimal direction that intersects with the minimum. Figure B.1. shows how these angles vary as a function of the total circulation,  $G$ , and the so-called 'step size' parameter,  $\gamma$ . As  $G$  increases, the constraint plane shifts away from the center of the spherical distribution. When  $\gamma$  is kept constant and  $G$  is increased, it is observed that

PGD shows better performance and on the contrary FW algorithm deflectes from its better path. The step size is resulted with no signature influences in a constant  $G$ . In overall sense, two methods show considerable performances, however, the PGD algorithm provides better quality for reaching the minimum. This is the reason of using projected gradient descent method in this study.

# Curriculum Vitae

Name Surname : Acar Çelik

E-mail : acarcelik@gmail.com

## Education:

2013–2018 Dokuz Eylül University, Dept. of Mechanical Eng.

2018–2021 İzmir Kâtip Çelebi University, Dept. of Mechanical Eng.

## Work Experience:

Jul. 2016 – Aug. 2016 Intern – CMS Jant ve Makina Sanayi A.Ş.

Aug. 2017 – Sep. 2017 Intern – Turkish Aerospace Industries, Inc.

Feb. 2020 – Sep. 2020 Visiting Researcher – Technion Israel Institute of Technology

## Publications:

### **a. Refereed conference proceedings**

1. Lityum-iyon bataryalarda faz deęişim malzemelerinin uygulanması

21st National Thermal Science and Technique Congress, Turkey, 2017

2. Experimental and numerical investigation of 18650 lithium-ion battery cells

7th Global Conference on Global Warming, Turkey, 2018

3. Investigation of Inverse Magnus Effect by Partial Circulation Control Elements:

Experimental Design

8th International Conference of Fluid Flow, Heat and Mass Transfer, Canada, 2021

### **b. Research articles in refereed journals**

1. Passive thermal management of the lithium-ion battery unit for a solar racing car

International Journal of Energy Research, 2019